electronics

Article

Study on Robust Path-Tracking Control for an Unmanned Articulated Road Roller Under Low-Adhesion Conditions

Wei Qiang [1,†], Wei Yu [2,†], Quanzhi Xu [1] and Hui Xie [1,*]

1 State Key Laboratory of Engines, Tianjin University, Yaguan Rd. 135, Tianjin 300350, China; qiangwei@tju.edu.cn (W.Q.); xuquanzhi@tju.edu.cn (Q.X.)
2 Department of Teaching Affairs, Tianjin Institute of Software Engineering, Binshui West Rd. 399, Tianjin 300387, China; yuwei@tjise.edu.cn
* Correspondence: xiehui@tju.edu.cn
† These authors contributed equally to this work.

Abstract: To enhance the path-tracking accuracy of unmanned articulated road roller (UARR) operating on low-adhesion, slippery surfaces, this paper proposes a hierarchical cascaded control (HCC) architecture integrated with real-time ground adhesion coefficient estimation. Addressing the complex nonlinear dynamics between the two rigid bodies of the vehicle and its interaction with the ground, an upper-layer nonlinear model predictive controller (NMPC) is designed. This layer, based on a 4-degree-of-freedom (4-DOF) dynamic model, calculates the required steering torque using position and heading errors. The lower layer employs a second-order sliding mode controller (SOSMC) to precisely track the steering torque and output the corresponding steering wheel angle. To accommodate the anisotropic and time-varying nature of slippery surfaces, a strong-tracking unscented Kalman filter (ST-UKF) observer is introduced for ground adhesion coefficient estimation. By dynamically adjusting the covariance matrix, the observer reduces reliance on historical data while increasing the weight of new data, significantly improving real-time estimation accuracy. The estimated adhesion coefficient is fed back to the upper-layer NMPC, enhancing the control system's adaptability and robustness under slippery conditions. The HCC is validated through simulation and real-vehicle experiments and compared with LQR and PID controllers. The results demonstrate that HCC achieves the fastest response time and smallest steady-state error on both dry and slippery gravel soil surfaces. Under slippery conditions, while control performance decreases compared to dry surfaces, incorporating ground adhesion coefficient observation reduces steady-state error by 20.62%.

Keywords: unmanned articulated road roller; road roller dynamics model; hierarchical cascaded controller; strong tracking unscented Kalman filter observer

Academic Editor: Felipe Jiménez

Received: 23 December 2024
Revised: 15 January 2025
Accepted: 16 January 2025
Published: 19 January 2025

Citation: Qiang, W.; Yu, W.; Xu, Q.; Xie, H. Study on Robust Path-Tracking Control for an Unmanned Articulated Road Roller Under Low-Adhesion Conditions. *Electronics* **2025**, *14*, 383. https://doi.org/10.3390/electronics14020383

1. Introduction

UARR plays a vital role in large-scale construction projects such as roadworks, tunnels, and dam engineering, attracting increasing interest from universities, research institutions, and manufacturers worldwide [1–5]. Their articulated structure affords high maneuverability; however, the drum's substantial mass and smooth steel surface compromise dynamic stability, particularly on uneven or wet, slippery surfaces [6–8]. In practical construction scenarios, path-tracking accuracy is pivotal, as it determines the quality of the compaction path. Any dynamic instability can divert the roller from its intended trajectory, impairing compaction performance and operational efficiency. Excessive lateral slip further poses safety risks in construction. Consequently, enhancing UARR path-tracking accuracy and stability under complex, low-adhesion road conditions has become a critical technical challenge.

Among the various control algorithms employed for UARR, PID control remains one of the most widely used. For instance, Zhang et al. [9] implemented PID feedback control in road rollers, but its reactive nature only applies corrections after significant tracking errors occur, often introducing “snaking motion” and reducing compaction quality. Bian et al. [10] improved upon this limitation by integrating fuzzy logic into PID control; however, rule design remains complex. Similarly, segmented PID parameter tuning still struggles with parameter adjustment in practice. In summary, traditional PID-based methods show clear constraints in achieving the stringent path-tracking requirements of UARR.

To address these challenges, a variety of model-based control algorithms have been explored. Song [11] proposed a composite disturbance rejection framework combining attitude correction, feedforward kinematic control, and an extended state observer (ESO) to handle external disturbances, nonlinearity, and uncertainties. Yet, reliance on purely geometric kinematics can overlook dynamic interactions between the roller and the ground. Xu [12] introduced a disturbance rejection controller (DRC) coupled with a modified pure pursuit controller (MPPC), which improved path tracking by estimating model errors and disturbances via an ESO. However, the ESO’s performance deteriorates under slippery or uneven surfaces given its dependence on simplified kinematics. Fang et al. [13] incorporated a dynamic model with drum vibrations to design a feedforward controller, but the framework remained too simplistic for the highly nonlinear UARR environment. Similarly, Yang et al. [7] employed a preview controller with side-slip compensation based on Kane’s method, improving steering angle adjustments in real time but neglecting variations in ground adhesion, thus limiting performance on wet and slippery terrain. Articulated road rollers inherently face challenges stemming from poor lateral stability and intricate ground interactions—factors exacerbated by uneven terrain, slopes, and slippery surfaces. These conditions often induce complex drum–body dynamics, which planar kinematic or simplified dynamic models fail to accurately capture. As a result, two-body system dynamics modeling provides a more robust foundation for high-precision UARR path-tracking and stability control.

Beyond UARR-specific investigations, several studies have explored path-tracking control strategies for various articulated vehicles. For instance, Deng [14] applied a linear quadratic regulator (LQR) based on a 3-DOF linear yaw plane model to track yaw rate and side-slip angle, thereby improving both low-speed maneuverability and high-speed stability. Similarly, Tian [15] proposed a fractional-order preview controller for the tractor section of articulated heavy vehicles (AHVs), simulating the driver’s varying visual clarity with distance to optimize front-wheel steering for enhanced path tracking and lateral stability at high speeds. For the trailer section, Tian introduced two strategies—a single-point preview controller for low-speed precision and an LQR approach for high-speed dynamic stability. Addressing lateral instability and rollover in high-speed AHVs, Mustafa A. [16] developed a lateral dynamic model based on a nonlinear framework. By linearizing this model, an active steering-based linear quadratic integral controller could be designed, accounting for variations in vehicle mass and simultaneously controlling both truck and trailer steering angles—an advancement over earlier work that primarily focused on trailer steering alone. Despite these progressions, many studies rely on linearized tire models, which may lead to significant errors under complex or unstructured road conditions. Sun [17] focused on underground articulated vehicles, introducing a two-layer nonlinear model predictive control (NMPC) scheme. The upper layer minimized path-tracking errors, while the lower layer converted controller outputs into executable commands. Though a terminal cost function enhanced closed-loop stability by aligning with low-speed characteristics, the approach remained limited by its reliance on a purely kinematic model. Tarun Sharma [18] tackled both path tracking and dynamic stability in AHVs using a 7-DOF nonlinear dynamic model that includes lateral, longitudinal, and yaw dynamics with a Dugoff tire model. Although real-time steering angle and drive torque optimization achieved high tracking accuracy, the assumption of a constant ground adhesion coefficient confines its suitability to relatively structured roads. Zhong [19] proposed a sliding-mode predictive controller for articulated vehicles on low-adhesion surfaces leveraging the robustness of sliding-mode control and the feedback correction of predictive control. However, the study linearized the tire model and did not explicitly incorporate real-time ground adhesion estimation, limiting its adaptability under highly uncertain or rapidly changing conditions. In contrast, Hu [20] developed an adaptive model predictive control approach for the path tracking of articulated tracked vehicles, aiming to address the system's nonlinearity and adaptability to complex environments. While this method enhances trajectory smoothness and control accuracy, it does not delve into the online estimation of the ground adhesion coefficient, leaving the impact of varying tire–ground friction on vehicle dynamics less explored. Taken together, these works highlight that simplified or fixed tire assumptions, along with the absence of real-time ground adhesion estimation, can restrict the precision and robustness of path-tracking control when encountering complex, unstructured terrains—a scenario routinely faced by UARR.

The real-time estimation of ground adhesion coefficients has been extensively explored through advanced filtering algorithms. For instance, Ji [21] proposed a soft-sensing approach based on the cubature Kalman filter, integrating the Dugoff tire model with a 3-DOF dynamic framework to achieve more accurate adhesion coefficient estimates. Qi [22] introduced a particle filter (PF) method utilizing a 7-DOF model alongside the Dugoff to estimate adhesion coefficients under various road conditions; a comparative study revealed the PF's superior accuracy, robustness, and control performance compared to the unscented Kalman filter (UKF). Quan [23] developed a high-order cubature Kalman filter incorporating an improved spherical radial numerical integration theory. By formulating state and measurement equations that account for slip ratios and side-slip angles, the algorithm demonstrated robust real-time performance in both high- and low-adhesion environments. Meanwhile, Li [24] proposed a data-driven approach combining CarSim simulations, real vehicle data, and deep learning techniques (e.g., self-attention, CNNs, and LSTMs), with reinforcement learning (Q-learning) used to optimize model parameters. Although effective for offline analysis and dataset-driven optimization, this framework is less suited to real-time estimation. For UARR in wet, uneven gravel soil conditions, the anisotropic nature of the ground imposes even greater challenges, as adhesion coefficients can vary dynamically during compaction. Consequently, observer designs must balance historical data weighting and real-time adaptability, ensuring robust performance under rapid and unpredictable changes.

In addition to these model-based approaches, recent studies in the passenger car domain have increasingly leveraged machine learning (ML) techniques—such as deep neural networks, reinforcement learning, and fuzzy neural controllers—to address path tracking and dynamic stability under a wide range of driving conditions. For instance, Xiao [25] proposed an extended dynamic mode decomposition (EDMD) method integrated with deep learning to model both longitudinal and lateral dynamics in autonomous vehicles. The resulting DE-MPC, built from the learned model, demonstrated excellent real-time performance and high control precision in trajectory tracking tasks. Similarly, Ma [26] developed a self-optimizing path-tracking controller based on deep reinforcement learning, aiming to tackle the challenges arising from highly dynamic and complex road conditions. By integrating reinforcement learning into traditional controllers, this approach improved adaptability to diverse trajectories and speed regimes, while also enabling online learning and optimization. The controller's robustness and generalization were further verified in complex environments. Focusing on efficiency, Wu [27] introduced a Fast Model Predictive Control (FMPC) method grounded in a Symmetric Saturation Linear Recurrent Neural Network (SSL-RNN) model, providing a high-precision and computationally efficient solution for autonomous vehicle trajectory tracking. J. Enrique Sierra-Garcia [28] proposed a hybrid control architecture that combines a Reinforcement Learning Controller (RLC) for path tracking with a conventional PI controller to maintain wheel speed, thereby enhancing the tracking performance of Automated Guided Vehicles (AGVs) on complex trajectories. Lastly, Yao [29] presented a path-tracking control strategy rooted in the deep deterministic policy gradient (DDPG) algorithm, further refined with a double critic network (DCN). This enhanced DDPG framework yielded significant improvements in both stability and accuracy for autonomous vehicle path-tracking tasks. Nevertheless, these ML-based approaches often impose high computational demands, which may be difficult to accommodate in large, specialized construction vehicles operating under intense vibrations and dust exposure. Furthermore, the dynamics of UARR are inherently more complex than those of passenger cars, and the data-driven nature of ML methods can require extensive, high-quality datasets that are challenging to collect in variable and hazardous work sites. Directly transferring ML algorithms from structured road environments to UARR applications may, thus, prove impractical. Consequently, there is a pressing need for alternative control frameworks that are explicitly tailored to UARRs' unique operational demands and robust enough to handle complex, unstructured ground.

A literature review indicates that although numerous path-tracking control algorithms have been proposed for UARR, most simplify the hydraulic system and tire dynamics or merely treat ground contact effects as disturbances. Since UARR is primarily tasked with compacting wet and slippery, the applicability and robustness of the existing control strategies in complex construction environments remain limited. While some studies have attempted to enhance path tracking by estimating the ground adhesion coefficient for general articulated vehicles, the structure and operating conditions of these vehicles differ significantly from those of a UARR. Additionally, the existing filtering algorithms for real-time ground adhesion estimation fail to adjust the weight of historical data, making them unsuitable for rapidly changing, unstructured terrain. Consequently, these approaches cannot effectively meet the practical demands of UARRs in dynamic, challenging environments.

To address these challenges, this study proposes an HCC framework that integrates real-time ground adhesion estimation to improve computational efficiency, control accuracy, and system robustness in adapting to environmental variations:

- Upper-layer NMPC: Leveraging a 4-DOF dynamics model, this controller effectively captures the complex nonlinear dynamics between the vehicle and the ground, computing the necessary steering torque to minimize position and heading errors.
- Lower-layer SOSMC: This controller precisely tracks the steering torque and outputs the corresponding steering angle, ensuring swift response and high-precision command execution while also reducing the NMPC's computational burden.
- ST-UKF Observer: Tailored to the anisotropic and time-varying nature of slippery surfaces, this observer enhances the real-time estimation of the ground adhesion coefficient by dynamically adjusting its covariance matrix. In so doing, it lessens the reliance on historical data and significantly boosts system adaptability under complex road conditions.

In this paper, Section 2 describes the real-vehicle experimental platform. Section 3 develops a 4-DOF dynamic model for the UARR using the Newton–Euler method (NEM), along with an articulated hydraulic system model and Dugoff-based tire models, capturing the longitudinal, lateral, and yaw motions of the drum as well as the relative oscillatory movement between the articulated bodies. In Section 4, the high nonlinearity of UARR dynamics is tackled by designing an HCC strategy that combines NMPC with SOSMC. In addition, an ST-UKF observer is introduced to address the anisotropic and rapidly changing nature of ground adhesion. Section 5 presents the performance verification and analysis of the proposed controller. Finally, the paper concludes with a summary of the findings.

2. The Experimental Platform

2.1. Real-Vehicle Testing Platform

This study utilizes a 22-ton articulated single-drum road roller, integrating perception, control, actuator, and remote monitoring systems to enable the comprehensive functionalities of sensing, decision making, planning, and control. The developed test platform serves as a foundation for the subsequent research efforts. The original vehicle parameters are provided in Table 1.

Table 1. Parameters of the original road roller.

Description	Parameter Value	Unit
Total Mass	22,000	kg
Drum Distributed Mass	14,600	kg
Rear Body Distributed Mass	7400	kg
Drum Static Linear Load	678	N/cm
Overall Length	6497	mm
Overall Width	2318	mm
Overall Height	3330	mm
Drum Diameter	1600	mm
Drum Width	2130	mm
Wheelbase	3182	mm
Steering Angle	±35	deg
Minimum Turning Radius	12,350	mm
Hydraulic Cylinder Length	455	mm
Hydraulic Cylinder Diameter	100	mm
Piston Rod Length	255	mm
Piston Rod Diameter	56.4	mm

Figure 1 illustrates the hardware distribution across various components. The perception system includes an integrated navigation module, wheel speed sensors, an articulation angle sensor, and both millimeter-wave and ultrasonic radars. The integrated navigation module, installed on the front frame of the drum, measures position, heading, and velocity. Combined with the articulation angle sensor, it determines the relative position of the rear body with respect to the drum. Wheel speed sensors provide angular velocity data for both the drum and the rear wheels, while the two radars collectively form a comprehensive obstacle avoidance system. The control system employs a custom-designed domain controller, developed specifically for the UARR and based on the AURIX TC397 platform, to handle all the control tasks. The actuator system consists of a longitudinal speed control motor, a lateral heading control motor, and their associated split controllers. The remote monitoring system integrates an onboard data radio, a remote end data radio, and an upper-level monitoring platform. This configuration enables the real-time transmission of vehicle status, task progress, and fault information while also allowing for remote task assignments to the UARR.

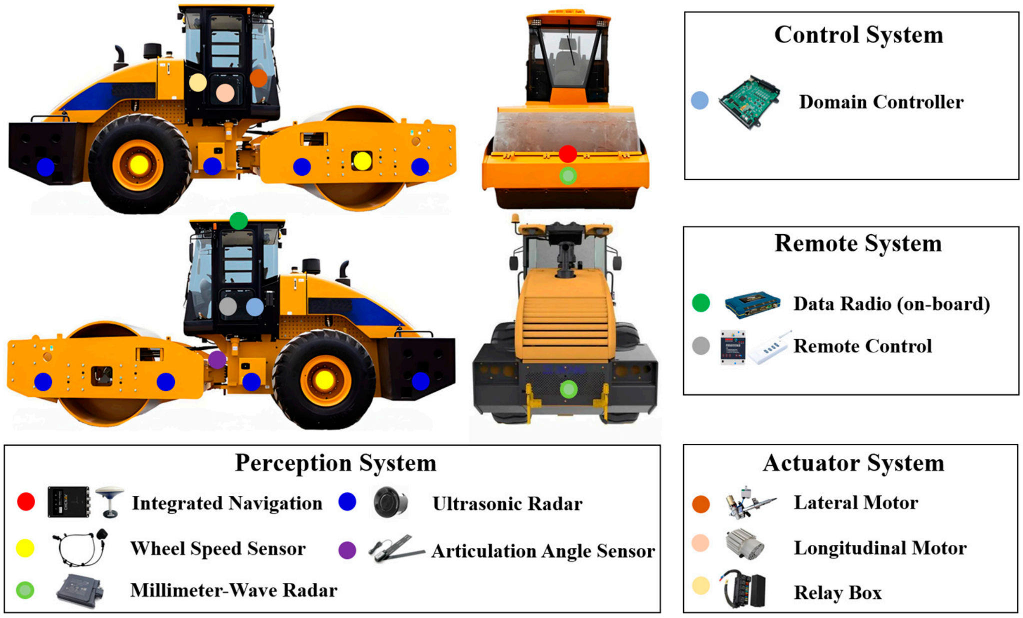

Figure 1. UARR hardware layout.

2.2. Simulation Platform

The road roller represents a highly complex dynamic system, combining an articulated structure, an engine, and a hydraulically driven hybrid power strategy. Traditional simulation tools such as TruckSim, TruckMaker, and Amesim often struggle to fully address the multi-domain simulation demands of such systems. Although multi-software co-simulation can enhance simulation capabilities, it inevitably introduces challenges, including integration complexity, data consistency issues, system stability concerns, increased computational resource demands, and reduced real-time performance.

To overcome these limitations, this study develops a physical model of an articulated single-drum road roller based on causal relationships. This approach aims to provide a robust multi-physics virtual platform, serving as a foundation for simulation testing. The model incorporates key components such as ground interactions, the drum, front and rear frames, rear wheels, the articulated mechanism, and the hydraulic system, as depicted in Figure 2.

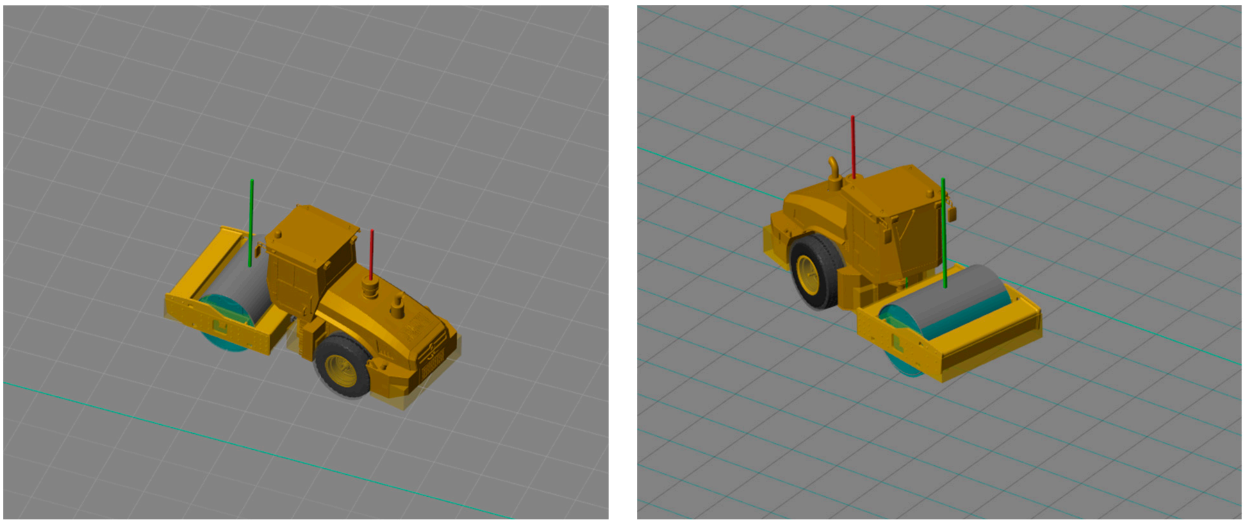

Figure 2. Causality-based modeling simulation platform for road roller.

3. UARR Dynamics Model

3.1. Force Analysis and Dynamics Modeling

The UARR is a highly nonlinear and strongly coupled system. To address the research objectives of this study while balancing model accuracy with the complexity of controller and observer design, a 4-DOF dynamics model is formulated using the NEM. This model aims to accurately capture the motion characteristics of the UARR based on the following assumptions:

- Neglecting vertical motion, only longitudinal and lateral translations, as well as yaw motion, are considered;
- Neglecting pitch and roll motion, the UARR is assumed to move strictly within a plane;
- Based on real vehicle measurements, $\sigma_{L/R2}$ is less than 5° and is, therefore, neglected
- Second bullet;
- The tire characteristics on both sides of the rear body are assumed to be identical, with the effects of camber angle and aligning torque neglected;
- As a low-speed road construction machine operating at approximately 3 km/h during uneven surface compaction, the effects of air resistance are considered negligible.

In summary, the 4-DOF dynamics model incorporates the drum's longitudinal and lateral translation, yaw motion about the z_1 axis, and the relative oscillation between the drum and the rear body.

As depicted in Figure 3a,b, the force analysis of the UARR is presented in both the 3D space and the 2D plane. The definitions of the symbols used in the figure are provided in Table 2.

Table 2. Definitions of symbols used in UARR modeling.

Symbol	Definition	Unit
J	Articulated point	—
F	Drum geometric center	—
CG_f	Drum gravity center	—
R	Rear body geometric center	—
CG_r	Rear body gravity center	—
F_{xf}, F_{yf}, F_{zf}	Drum longitudinal, lateral, and vertical force, respectively	N
F_{xf}, F_{yf}, F_{zf} ($i = 1, 2$)	Rear wheel longitudinal, lateral, and vertical force, respectively. $i = 1$ is left rear wheel and $i = 2$ is right	N
F_L, F_R	Hydraulic cylinder force	N
C_X, C_Y, C_Z	Interaction force at the articulation point along the drum's x_1, y_1, and z_1 axes	N
v_{xj}, v_{yj}, v_{zj} ($j = 1, 2$)	Rigid body velocity along x_j, y_j, and z_j axes; $j = 1$ drum, $j = 2$ rear body	m/s
$\omega_{xj}, \omega_{yj}, \omega_{zj}$ ($j = 1, 2$)	Rigid body angular velocity along x_j, y_j, and z_j axes; $j = 1$ drum, $j = 2$ rear body	rad/s
$L_{f1}, L_{f2}, L_{r1}, L_{r2}$	Distances from CG_f/CG_r to F/R and J	m
a, b, c, d, e	Hydraulic cylinder connection distances on UARR	m
α_1, α_2	Drum and rear wheel slip angles	rad
β_1, β_2	Drum and rear body slip angles	rad
$\sigma_{L/Rk}$ ($k = 1, 2$)	Angle between the hydraulic cylinder and drum/rear body axis. $k = 1$ left hydraulic cylinder and $k = 2$ is right	rad
δ	Articulation angle	rad

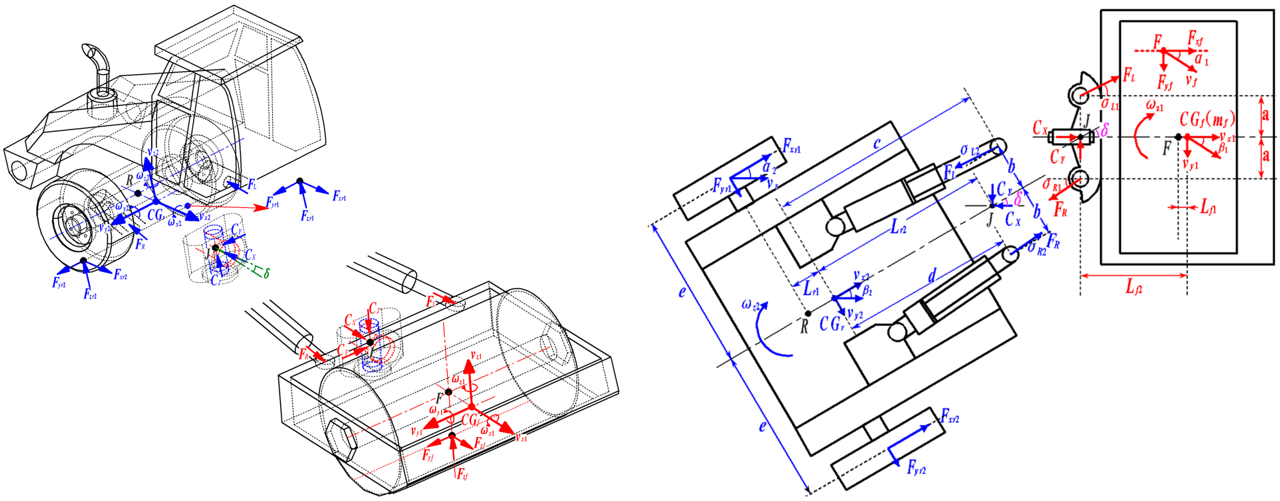

(**a**) (**b**)

Figure 3. Force analysis of UARR dual bodies: (**a**) 3D force analysis; (**b**) planar force analysis and structural parameters.

In Figure 3, the force balance equations along the x_1 and y_1 axes and the moment balance equation about the z_1 axis for the drum are established using the NEM:

$$\begin{cases} m_f(\dot{v}_{x1} - v_{y1}\omega_{z1}) = F_{xf} + (F_L - F_R)\cos\delta + C_X \\ m_f(\dot{v}_{y1} + v_{x1}\omega_{z1}) = F_{yf} - (F_L - F_R)\sin\delta - C_Y \\ I_{z1}\dot{\omega}_{z1} = -F_{yf}L_{f1} + a(F_L + F_R)\cos\delta + L_{f2}(F_L - F_R)\sin\delta + C_Y L_{f2} \end{cases} \quad (1)$$

For the rear body, three equations are established along the x_2, y_2, and z_2 axes:

$$\begin{cases} m_r(\dot{v}_{x2} - v_{y2}\omega_{z2}) = (F_{xr1} + F_{xr2}) - (F_L - F_R) - (C_X\cos\delta + C_Y\sin\delta) \\ m_r(\dot{v}_{y2} + v_{x2}\omega_{z2}) = (F_{yr1} + F_{yr2}) - (C_X\sin\delta - C_Y\cos\delta) \\ I_{z2}\dot{\omega}_{z2} = e(F_{xr1} - F_{xr2}) - L_{r1}(F_{yr1} + F_{yr2}) - b(F_L + F_R) - L_{r2}(C_X\sin\delta - C_Y\cos\delta) \end{cases} \quad (2)$$

Here, m_f and m_r are the masses of the drum and rear body, respectively, while I_{z1} and I_{z2} denote the moments of inertia about the z_j (j = 1, 2) axes. The parameter values are listed in Table 3.

$$\begin{cases} m_f a_{fx} = m_f(\dot{v}_{x1} - v_{y1}\omega_{z1}) \\ m_f a_{fy} = m_f(\dot{v}_{y1} + v_{x1}\omega_{z1}) \\ m_r a_{rx} = m_r(\dot{v}_{x2} - v_{y2}\omega_{z2}) \\ m_r a_{ry} = m_r(\dot{v}_{y2} + v_{x2}\omega_{z2}) \end{cases} \quad (3)$$

Table 3. Measured parameter values in dynamic equations.

Parameter	Value	Unit
m_f	16,400	kg
m_r	7400	kg
JF	1500	mm
JR	1600	mm
$a = b$	230	mm
e	1050	mm
δ	±35	deg

Here, a_{fx}, a_{fy}, a_{rx}, and a_{ry} represent the accelerations of the drum and the rear body, respectively.

Given the constraint at articulation point J, the velocities of the front and rear bodies must align. From this condition, the longitudinal velocity v_{x2} and lateral velocity v_{y2} are derived as follows:

$$\begin{cases} v_{x2} = v_{x1}\cos\delta - v_{y1}\sin\delta + L_{f2}\omega_{z1}\sin\delta \\ v_{y2} = v_{x1}\sin\delta + v_{y1}\cos\delta - L_{f2}\omega_{z1}\cos\delta - L_{r2}\omega_{z2} \end{cases} \tag{4}$$

Differentiating Equation (4) yields the rear body acceleration as follows:

$$\begin{cases} \dot{v}_{x2} = \dot{v}_{x1}\cos\delta - (\dot{v}_{y1} - L_{f2}\dot{\omega}_{z1})\sin\delta - (v_{x1}\sin\delta + v_{y1}\cos\delta - L_{f2}\omega_{z1}\cos\delta)\dot{\delta} \\ \dot{v}_{y2} = \dot{v}_{x1}\sin\delta + (\dot{v}_{y1} - L_{f2}\dot{\omega}_{z1})\cos\delta - L_{r2}\dot{\omega}_{z2} + (v_{x1}\cos\delta - v_{y1}\sin\delta + L_{f2}\omega_{z1}\sin\delta)\dot{\delta} \end{cases} \tag{5}$$

Additionally, the relationship between the δ and the angular velocities of the dual-body z_j (j = 1, 2) axes is given by the following:

$$\dot{\delta} = \omega_{z1} - \omega_{z2} \tag{6}$$

By substituting Equations (4)–(6) into the rear body dynamic differential Equation (2) and combining it with the drum Equation (1), the interaction forces C_X and C_Y at articulation point J are eliminated. The resulting nonlinear dynamic model of the UARR is expressed as follows:

$$A\dot{X} + bu + f(x) = 0 \tag{7}$$

Here, $\dot{X}$ represents the state variable, $u = M_j$ is the control input, and $f(x)$ denotes the nonlinear term, as detailed in Appendix A.

For the nonlinear dynamic model of the UARR represented by Equation (7), F_{xf}, F_{yf}, F_{xri}, and F_{yri} (i = 1, 2), and the moment M_j are provided by the tire model and hydraulic steering model discussed in the subsequent sections.

3.2. Tire Modeling

The tire model is classified into linear and nonlinear categories [30]. In a linear model [31], the tire's lateral force is proportional to the slip angle within a small range, simplifying its structure and reducing parameters. This makes it suitable for state estimation and controller design. However, on wet and slippery surfaces with anisotropic adhesion, the linear model often produces significant errors, causing failures in controllers and observers, and limiting its practical applicability. In contrast, nonlinear models [32,33], such as the Dugoff model [34], Magic Formula [35–37], and Brush model [38], provide greater accuracy and better capture the tire's complex mechanical characteristics. To balance accuracy and computational complexity in the controller and observer design, this study adopts the Dugoff tire model. By explicitly incorporating the adhesion coefficient, the Dugoff achieves moderate complexity, fewer parameters, and easier system identification, making it well suited for challenging conditions like slippery road surfaces.

However, the applicability of the Dugoff to steel rollers still requires further research and investigation. Reference [39] systematically investigates the frictional characteristics at the sand–steel pipe jacking interface under various working conditions, revealing a nonlinear relationship between shear stress and shear displacement. It further examines the effects of normal stress and lubrication on shear stress. Notably, shear stress represents the shear force per unit area, governed by interface friction. In the UARR system, the steel drum operates on a gravel surface with particles of varying sizes. Consistent with the setup in the above Reference, the lateral and longitudinal forces at the drum interface arise from friction and correlate with the shear force. This alignment provides a theoretical basis for applying the Dugoff tire model. Shear displacement represents the relative sliding between the steel surface and sand under shear action. As shear displacement increases, the interface transitions from adhesion to sliding, corresponding to the slip ratio or slip angle of the drum, which similarly describes relative motion. Thus, shear displacement and slip ratio or slip angle share a comparable physical interpretation, both reflecting interface motion characteristics.

Figure 4 shows that the Dugoff accurately captures the shear stress–shear displacement relationship. The fitting results reveal a strong correlation between the shear behavior of sand particles and the nonlinear response captured by the Dugoff, characterized by an initial sharp rise to a peak, followed by gradual softening and stabilization. These features reflect the transition from static to dynamic friction and the effects of particle embedding, sliding, and interfacial interactions.

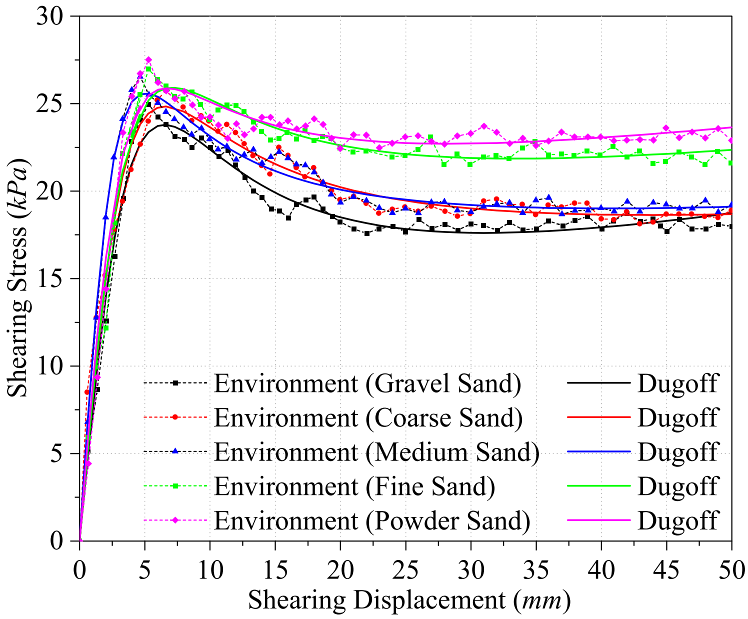

Figure 4. Fitting the Dugoff model to shearing stress–shearing displacement data [39].

Despite differences in material composition and geometry between the drum and tire, the fundamental slip-friction mechanism remains consistent. This consistency establishes a foundation for extending the Dugoff to describe the lateral force–slip angle relationship in the drum and contact surface system. To further validate the applicability of the Dugoff model to the drum, both real-vehicle and simulation tests were conducted for comparison. In the experiments, the vehicle speed was set to 3 m/s, and the steering wheel was rotated 650° to complete a circular path while recording the latitude and longitude coordinates of the drum's center of mass. The comparison between the simulation and experimental results, as shown in Figure 5, yields a correlation coefficient of 89.72%, further confirming the applicability of the Dugoff model to the drum.

The drum and rear wheel models can be represented through Equations (A5)–(A10) [24,40,41], as detailed in Appendix A.

In the above equations, S_{xf} denotes the longitudinal slip ratio of the drum, and S_{xri} (i = 1 for the left wheel, i = 2 for the right wheel) represents the longitudinal slip ratio of the rear tires. $C_{yf/r}$ and $C_{xf/r}$ are the lateral and longitudinal stiffness of the drum and rear wheels, respectively, while $F_{zf/r}$ are the normal forces acting on the drum and rear body. $f(\kappa)$, a nonlinear function, is used to describe the variation in tire force as the slip ratio transitions from linear to nonlinear saturation. When $\kappa \geq 1$, the tire force reaches a saturated state, whereas for $\kappa < 1$, the tire force is in the transition region between linear and nonlinear behavior. κ represents a nonlinear parameter derived by neglecting the influence of wheel slip velocity on wheel force. R_f and R_r are the radii, and ω_f and ω_r are the rotational speeds of the drum and rear wheels, respectively. Finally, μ, the ground adhesion coefficient, is discussed in detail in the adhesion coefficient observer section.

We normalized $F_{xf/ri}$ and $F_{yf/ri}$:

$$F_{yf/ri} = \mu_{f/ri} F^0_{yf/ri} = \mu_{f/ri} F_{zf/r} C_{yf/r} \frac{\tan(\alpha_{1/2})}{1 - S_{xf/ri}} f(\kappa) \tag{8}$$

$$F_{xf/ri} = \mu_{f/ri} F^0_{xf/ri} = \mu_{f/ri} F_{zf/r} C_{xf/r} \frac{S_{xf/ri}}{1 - S_{xf/ri}} f(\kappa) \tag{9}$$

Here, $F^0_{xf/ri}$ and $F^0_{yf/ri}$ represent the normalized longitudinal and lateral forces, respectively, and are functions of $S_{xf/ri}$, $F_{zf/r}$, and $\tan(\alpha_{1/2})$, independent of $\mu_{f/ri}$. This form aids in estimating the adhesion coefficient.

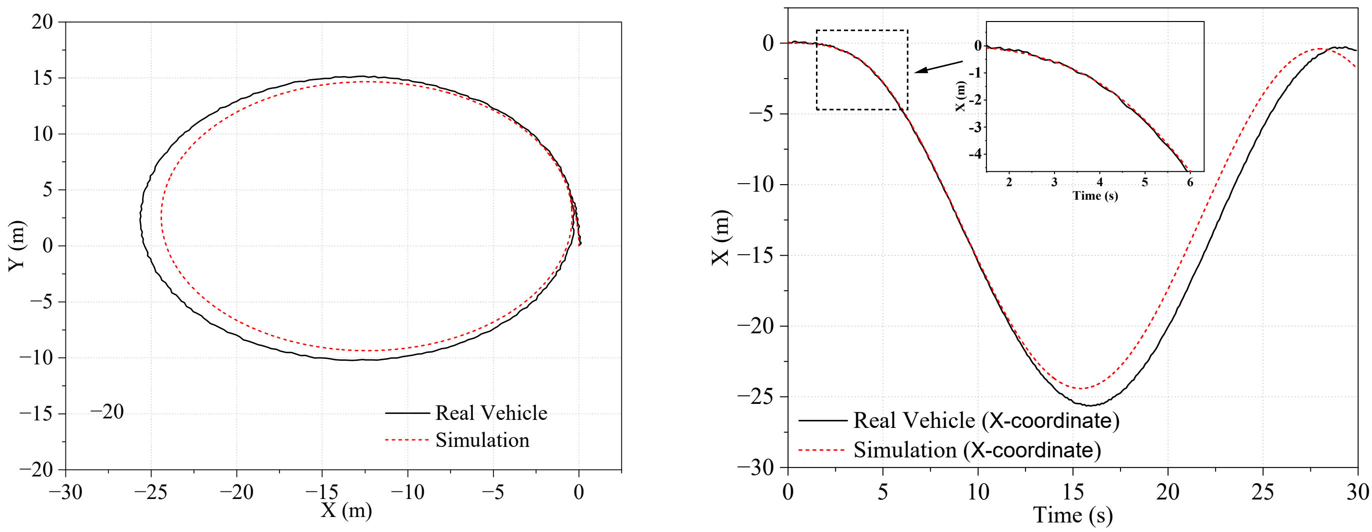

(**a**) (**b**)

Figure 5. Feasibility verification of the Dugoff model for the drum: (**a**) circular test; (**b**) X coordinate.

3.3. Hydraulic Steering System Modeling

The UARR hydraulic steering system consists of key components, including the steering gear, hydraulic cylinders on either side of the articulation point, the reservoir, and the gear pump. Figure 6 shows an equivalent schematic diagram, with the orange lines indicating the oil flow from the reservoir to the hydraulic cylinders and the blue lines representing the return flow.

The steering gear forms the core of the system, comprising the valve body, valve spool, valve sleeve, and cycloidal motor. The steering column is spline-coupled to the valve spool, transmitting the steering wheel's rotation directly to the valve spool. Meanwhile, the valve sleeve connects to the cycloidal motor via a gear, enabling precise hydraulic control. The valve spool and sleeve are pinned together, and as the steering wheel rotates, the aligned grooves on the spool and ports on the sleeve create adjustable throttling openings (C_1 to C_5). Adjusting these openings controls the oil pressure to the hydraulic cylinders, thereby regulating the thrust or pull generated.

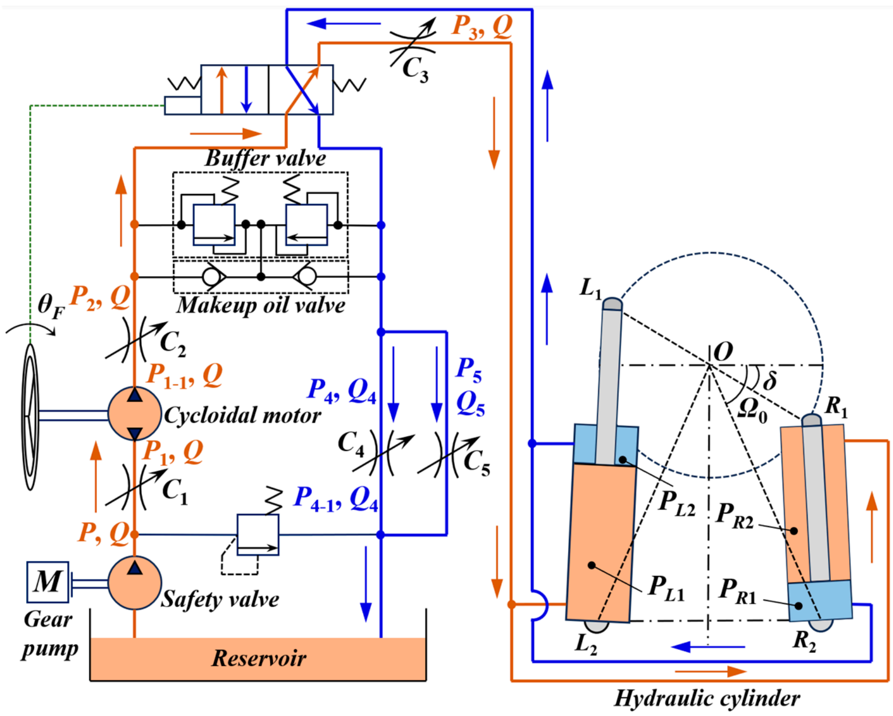

Figure 6. Equivalent schematic of the UARR hydraulic steering system.

Figure 7, the fixed bore of the valve spool is larger than that of the valve sleeve, resulting in a relative displacement between the steering wheel–steering column–valve spool assembly and the valve sleeve–cycloidal motor rotor assembly. Initially, as the steering wheel rotates, the valve spool follows, but this relative displacement is constrained. Once the limit is reached, the valve sleeve moves together with the spool. Let θ_F represent the steering wheel angle, θ_m the valve sleeve angle, D the valve spool diameter, and Φ_1 and Φ_2 the fixed bores of the valve spool and valve sleeve, respectively. The relative displacement Δx is given by the following:

$$\Delta x = \frac{D}{2}(\theta_F - \theta_m) \leq \frac{\Phi_1 - \Phi_2}{2} \tag{10}$$

Based on the continuity equation and Bernoulli's principle, the flow characteristics of the throttling openings C_1 to C_5 can be expressed as follows:

$$P = P_3 + \frac{\rho Q^2}{2C_d^2}\left(\frac{1}{A_{C1}^2} + \frac{1}{A_{C2}^2} + \frac{1}{A_{C3}^2}\right) + \frac{Q - D_m\dot{\theta}_m}{C_\Sigma} \tag{11}$$

$$Q = C_d A_{C4}\sqrt{\frac{2}{\rho}(P_4 - P_{4-1})} + C_d A_{C5}\sqrt{\frac{2}{\rho}(P_3 - P_4)} \tag{12}$$

In the above equations, P, P_3, P_4, and P_{4-1} represent the pressures before and after the related throttle orifice. The inlet pressure is $P = 12\,\text{MPa}$, and the reservoir back pressure is $P_{4-1} = 2\,\text{bar}$. Q represents the total flow rate from throttling orifices C_4 and C_5, which is the combined flow returning to the reservoir. A_{C1} to A_{C5} denote the areas of the throttle orifices, C_d is the flow coefficient, C_Σ is the total leakage coefficient of the cycloidal motor, and ρ is the hydraulic oil density. D_m is the theoretical angular displacement of the cycloidal motor.

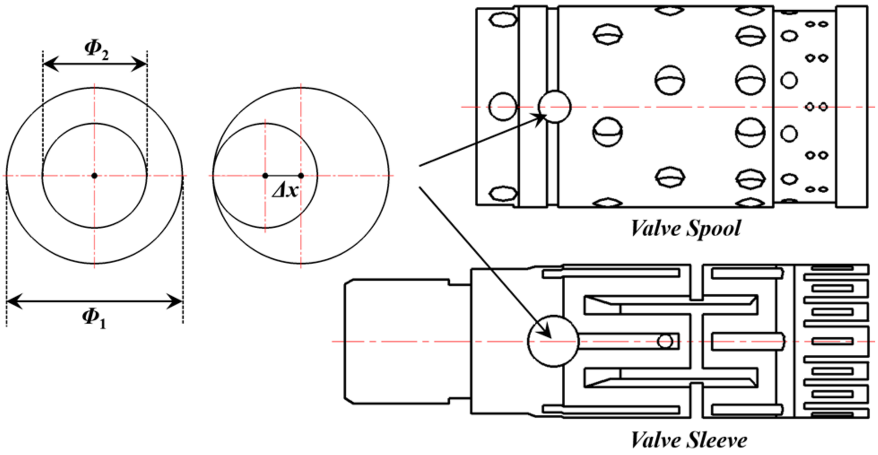

Figure 7. Relative displacement between the valve spool and valve sleeve.

Figure 8 shows a schematic diagram of the hydraulic cylinder's movement. Combined with the flow and pressure schematic of the hydraulic cylinder in the right part of Figure 4, the hydraulic oil entering the cylinder can be divided into three components: the volume change in the oil chamber caused by piston rod movement, the volume change induced by the compression of the hydraulic oil, and the oil leakage. Q_{L1} and Q_{R2} represent the flow rates entering the rodless chamber of the left hydraulic cylinder and the rod chamber of the right hydraulic cylinder, respectively, and are given by the following equations:

$$\begin{cases} Q_{L1} = A_1 \frac{d\Delta L_{left}}{dt} + C_{ci}(P_3 - P_4) + \frac{V_{L1}}{K_{MB}} \frac{dP_{L1}}{dt} \\ Q_{R2} = A_2 \frac{d\Delta L_{right}}{dt} + C_{ci}(P_3 - P_4) + \frac{V_{R2}}{K_{MB}} \frac{dP_{R2}}{dt} \end{cases} \tag{13}$$

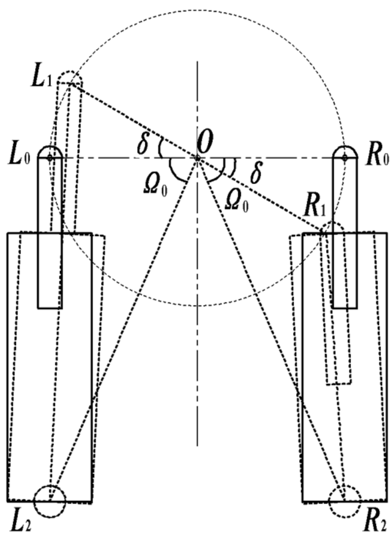

Figure 8. Principle diagram of piston rod movement.

Similarly, Q_{L2} and Q_{R1} can be expressed as follows:

$$\begin{cases} Q_{L2} = A_2 \frac{d\Delta L_{left}}{dt} + C_{ci}(P_3 - P_4) - \frac{V_{L2}}{K_{MB}} \frac{dP_{L2}}{dt} \\ Q_{R1} = A_1 \frac{d\Delta L_{right}}{dt} + C_{ci}(P_3 - P_4) - \frac{V_{R1}}{K_{MB}} \frac{dP_{R1}}{dt} \end{cases} \tag{14}$$

In the above two equations, A_1 and A_2 are the effective cross-sectional areas of the rodless and rod chambers, respectively. $d\Delta L_{left}/dt$ and $d\Delta L_{right}/dt$ represent the linear velocities of the piston rod relative to the hydraulic cylinder, while C_{ci} is the internal leakage coefficient. P_3 and P_4 are the outlet and inlet pressures of C_3 and C_4, respectively. P_{L1}, P_{R1}, P_{L2}, and P_{R2} denote the oil pressures in the rodless and rod chambers. K_{MB} is the modulus of elasticity of the hydraulic oil, and V_{L1}, V_{R2}, V_{L2}, and V_{R1} are the respective chamber volumes.

Furthermore, the system of differential equations for the hydraulic cylinder pressures P_3 and P_4, can be derived as follows:

$$\begin{cases} \frac{dP_3}{dt} = \frac{K_{MB}}{V_1}\left(Q - (A_1 h_{left} + A_2 h_{right})\dot{\delta} - 2C_{ci}(P_3 - P_4)\right) \\ \frac{dP_4}{dt} = \frac{K_{MB}}{V_2}\left(-Q + (A_2 h_{left} + A_1 h_{right})\dot{\delta} + 2C_{ci}(P_3 - P_4) + C_d A_{C5}\sqrt{\frac{2}{\rho}(P_3 - P_4)}\right) \end{cases} \quad (15)$$

where V_1 and V_2 are as follows:

$$\begin{cases} V_1 = (V_{0L1} + V_{0R2}) + (A_1 \cdot \Delta L_{left} + A_2 \cdot \Delta L_{right}) \\ V_2 = (V_{0L2} + V_{0R1}) - (A_2 \cdot \Delta L_{left} + A_1 \cdot \Delta L_{right}) \end{cases} \quad (16)$$

where V_{0L1}, V_{0R2}, V_{0L2}, and V_{0R1} are the initial chamber volumes, and h_{left} and h_{right} are the lever arms of the left and right hydraulic rods.

To express the hydraulic force, assuming the friction due to piston rod movement is negligible, the equation can be written as follows:

$$\begin{cases} F_L = P_3 A_1 - P_4 A_2 \\ F_R = P_4 A_2 - P_3 A_1 \end{cases} \quad (17)$$

Since $a = b$ in Figure 3b, the moment M_j can be expressed as follows:

$$M_j = a(F_L + F_R)\cos\delta \quad (18)$$

Thus, using the developed wheel and hydraulic models, the forces F_{xf}, F_{yf}, F_{xri}, and F_{yri} (i = 1, 2), and the moment M_j can be computed. Integrating these with Equation (7) establishes the comprehensive dynamics model.

3.4. Dynamics Model System Identification and Validation

The Non-dominated Sorting Genetic Algorithm II (NSGA-II) [42,43], incorporating an elitist strategy, is a widely used evolutionary algorithm for multi-objective optimization, known for its robust global search capabilities and strong convergence properties. In the developed UARR 4-DOF dynamic model, several system parameters remain unknown despite the availability of reference data and measurable parameters. These unknowns include the lateral and longitudinal stiffness of the drum and rear wheels (C_{yf}, C_{yr}, C_{xf}, and C_{xr}), the moments of inertia of the drum and rear body (I_{z1} and I_{z2}), and the distances from the drum and rear body centers of mass to the articulated joint (L_{f2} and L_{r2}). To effectively identify these parameters, a multi-objective optimization problem is defined to minimize the discrepancy between the model outputs and experimental measurements, with each discrepancy formulated as an objective function.

$$\begin{cases} J_1 = \sum_{i=1}^{N}\left[x_f^{meas}(t) - x_f^{model}(t)\right]^2 \\ J_2 = \sum_{i=1}^{N}\left[y_f^{meas}(t) - y_f^{model}(t)\right]^2 \\ J_3 = \sum_{i=1}^{N}\left[\varphi_{z1}^{meas}(t) - \varphi_{z1}^{model}(t)\right]^2 \end{cases} \quad (19)$$

Here, $x_f^{meas}(t)$ and $y_f^{meas}(t)$ are the measured coordinates of the drum's center of mass in the earth-fixed frame, and $\varphi_{z1}^{meas}(t)$ is the measured yaw angle. $x_f^{model}(t)$, $y_f^{model}(t)$, and $\varphi_{z1}^{model}(t)$ are the corresponding model estimates.

The algorithm flow is as follows:

- System Parameter Encoding: System parameters to be identified are encoded as chromosome vectors: $[C_{yf}, C_{yr}, C_{xf}, C_{xr}, I_{z1}, I_{z2}, L_{f2}, L_{r2}]$.
- Initial Population Generation: A random initial population is generated, with each individual representing a set of candidate parameter solutions, constructed from various combinations of the parameters listed.
- Fitness Evaluation: Multiple error objective functions J_1, J_2, and J_3 are defined to evaluate the fitness of each individual, addressing the multi-objective optimization nature.
- Non-dominated Sorting: Individuals in the population undergo non-dominated sorting, which assigns them to different front layers based on dominance relationships.
- Elitism Strategy: Elite individuals from the previous generation are retained in each iteration.
- Crowding Distance Calculation: Within each front layer, diversity is maintained by calculating the crowding distance.
- Crossover and Mutation: Crossover and mutation operations are applied to the population to generate new candidate solutions.
- Termination Criteria and Solution Selection: Upon reaching the termination condition, individuals from the first front layer of the final generation are selected as Pareto optimal solutions.
- Parameter Selection: From the Pareto optimal solutions, individuals with smaller errors and greater crowding distances are chosen for system identification.

To validate the accuracy of the 4-DOF dynamics model, on-road tests were performed on two typical unstructured road surfaces: a wet, slippery dirt road and a gravel road. A sensor system mounted on the UARR collected real-time data on key dynamic parameters, including yaw angle, yaw rate, and the latitude and longitude coordinates of the drum's center of mass. The model's estimated values were then compared with the measured data, followed by a fitting analysis, as shown in Figures 9–12.

1. Yaw Angle and Yaw Rate:

Yaw angle and yaw rate are critical state variables in the UARR dual-body dynamics model, directly influencing vehicle dynamics and control performance. To validate the model's prediction accuracy, real tests were conducted on two conditions: a wet dirt road and a gravel surface. Figures 9 and 10 present the two tests, with correlation coefficients of 95.58% and 97.22%, respectively. These high correlation values indicate that the dynamics model demonstrates strong predictive accuracy across different unstructured surfaces, effectively capturing the yaw angle and yaw rate characteristics of the drum under wet road conditions.

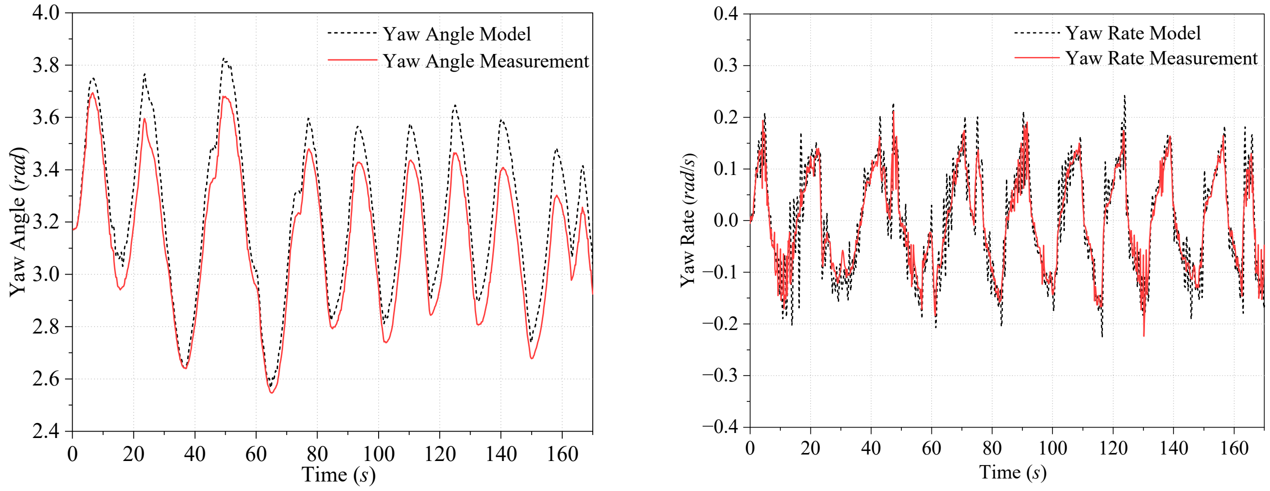

(**a**) (**b**)

Figure 9. Validation of the dynamics model on wet dirt road: (**a**) yaw angle; (**b**) yaw rate.

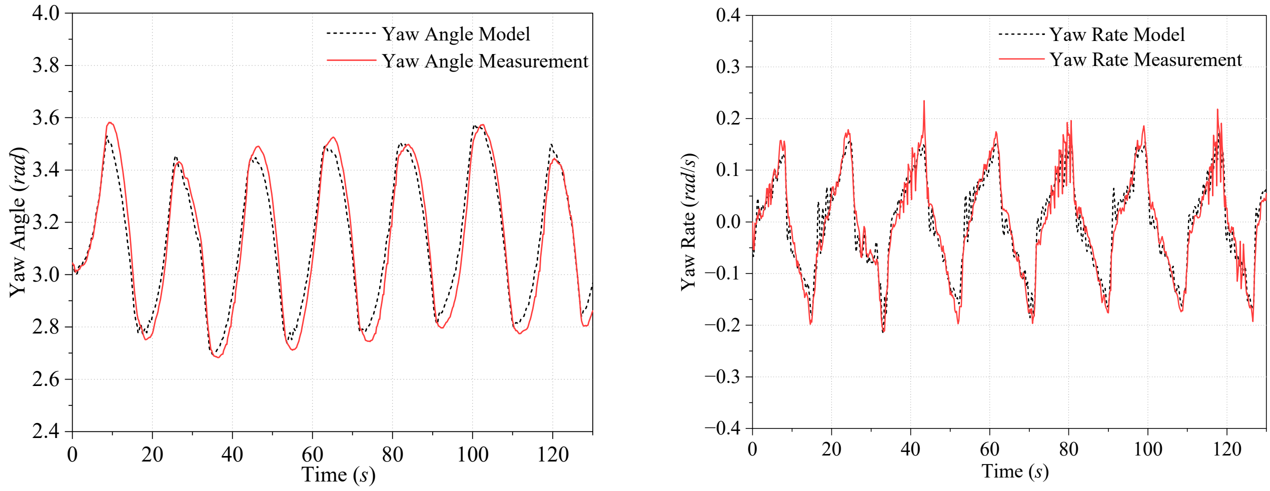

(**a**) (**b**)

Figure 10. Validation of the dynamics model on wet gravel road: (**a**) yaw angle; (**b**) yaw rate.

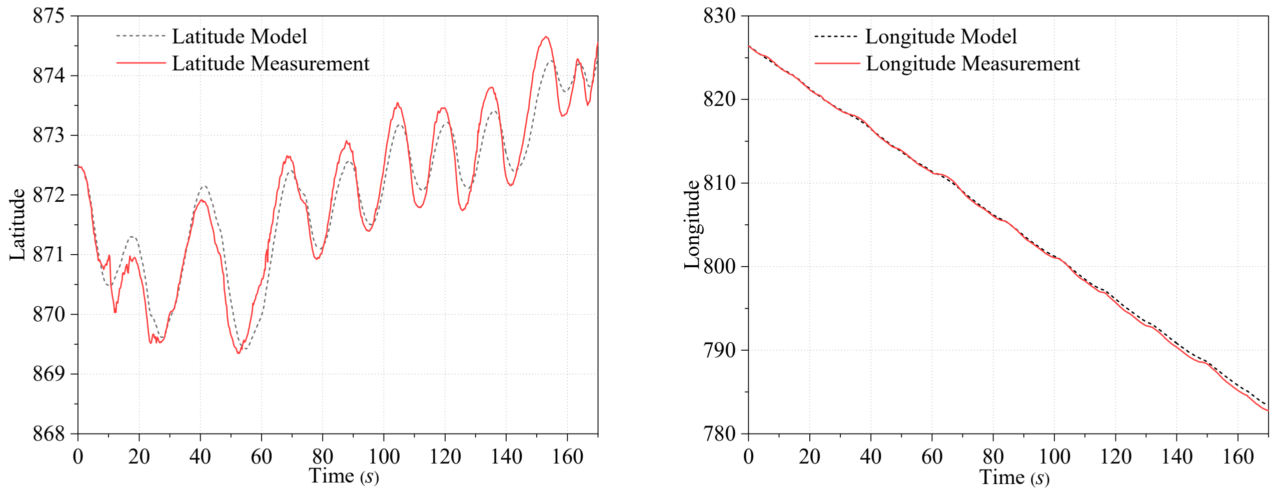

(**a**) (**b**)

Figure 11. Validation of the dynamics model on wet dirt road: (**a**) drum centroid latitude; (**b**) drum centroid longitude.

2. Drum Center Latitude and Longitude:

Figures 11 and 12 illustrate the model validation results for the latitude and longitude coordinates of the drum's center of mass. In the wet dirt road test, the correlation coefficients between the model estimates and experimental data were 92.84% for latitude and 97.18% for longitude. In the wet gravel road test, the correlation coefficients for the latitude and longitude coordinates were 91.81% and 97.59%, respectively.

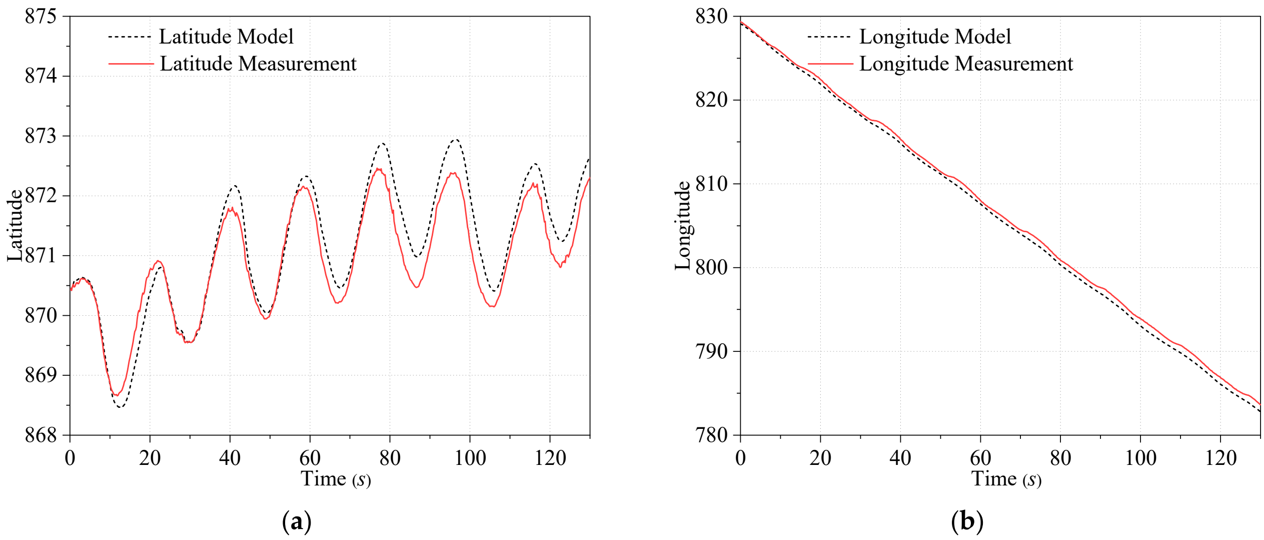

Figure 12. Validation of the dynamics model on wet gravel road: (**a**) drum centroid latitude; (**b**) drum centroid longitude.

4. UARR Lateral Slip Control

4.1. Hierarchical Cascaded Control Strategy Architecture

The front body, located at the articulation point, has a mass twice that of the rear body, resulting in a "front-heavy" configuration. Such a design is intended to fulfill the specific engineering requirements of road rollers. The drum, fabricated from pure steel, demonstrates low friction characteristics. Under reduced adhesion conditions, this configuration is prone to significant lateral slippage, subsequently causing the rear body to be dragged. Therefore, effective control of the UARR to mitigate such pronounced lateral slippage constitutes a significant research challenge—one that is vital for reducing construction-associated risks and enhancing overall operational efficiency.

Given the highly nonlinear nature of UARR dynamics, complex modeling introduces significant uncertainty and dynamic complexity, which pose major challenges for control. Furthermore, variations in the adhesion coefficient can critically impact control performance. To address these challenges, a hierarchical cascaded control framework is proposed, integrating NMPC with SOSMC, enhanced by an online estimation mechanism for the adhesion coefficient. The overall architecture, depicted in Figure 13, comprises two main components: a path-tracking controller and an online adhesion observer. The former employs a cascaded structure. The upper layer uses NMPC, formulated based on the UARR dynamics error model, to calculate the required steering torque from the position and heading errors. The lower layer then leverages SOSMC to accurately track the steering torque M_j provided by the upper layer, ultimately determining the corresponding steering wheel angle. This cascaded configuration significantly alleviates the computational demands of NMPC during online optimization, thereby improving the real-time responsiveness of the control system while maintaining precise path tracking. Meanwhile, the online adhesion observer employs the ST-UKF. This observer enhances lateral control adaptability and robustness, enabling the UARR to effectively navigate regions of pronounced slippage.

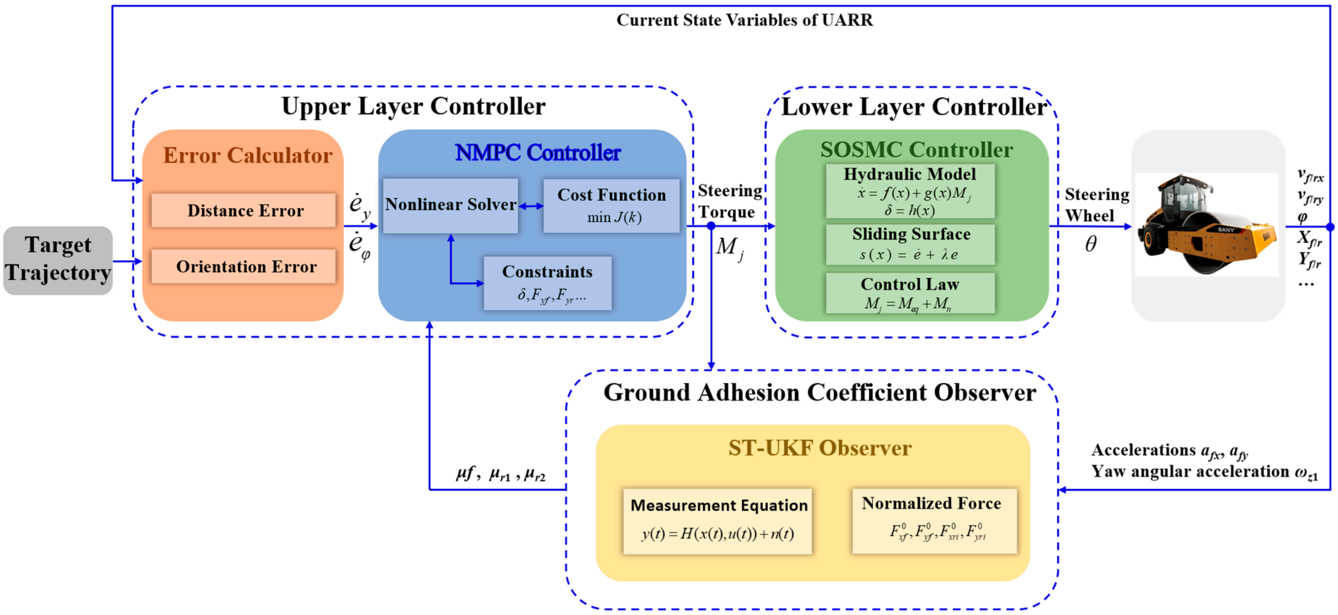

Figure 13. Hierarchical cascaded framework integrating NMPC and SOSMC with adhesion coefficient estimation.

4.2. NMPC Upper-Layer Controller

The lateral motion control problem involves multiple state variables and a single control output, classifying it as a multi-objective dynamic optimization problem. In designing the control objectives, precise tracking of the reference path must be ensured by minimizing path errors. Additionally, smooth vehicle operation is required, which necessitates minimizing the rate of change in the control input. Based on these considerations, a quadratic cost function is formulated in this paper as follows:

$$\min \int_{t_k}^{t_k+t_h} \left(\left\| x_{ref}(t) - x(t) \right\|_Q^2 + \|u(t)\|_{R_m}^2 + \|\Delta u(t)\|_{R_{\Delta m}}^2 \right) dt \tag{20}$$

Here, x_{ref} (t) represents the reference path at the current time, i.e., the desired state, while x(t) represents the actual state. The control input is u (t) = $M_j(t)$, and the change rate in the control input is Δu (t) = $\Delta M_j(t)$. The weight coefficient Q determines the controller's sensitivity to tracking errors during optimization, R_m controls the control input magnitude, and ΔR_m defines the smoothness of changes in the control input. In the cost function, the first term ensures the precise tracking of the desired path. The second term limits the control signal amplitude to prevent excessive input, avoiding unnecessary energy consumption and ensuring system stability. The third term emphasizes smooth changes in the control input to prevent abrupt variations, which is especially crucial under slippery road conditions where sudden steering torque could lead to instability.

To prevent excessive torque variations, appropriate inequality constraints are applied to the control input. Based on the estimates from Reference [44], the constraints are as follows:

$$-170 \text{ kNm} \leq M_j(t) \leq 170 \text{ kNm} \tag{21}$$

Additionally, the physical limitations of the steering mechanism are considered as follows:

$$-35\text{deg} \leq \delta(t) \leq 35\text{deg} \tag{22}$$

From the hydraulic system modeling analysis, a nonlinear mapping exists between the articulation angle and the steering wheel angle. Considering the physical limitations of the steering motor used in this study and experimental results, the constraint on the articulation angle rate is as follows:

$$-5.5\text{deg/s} \leq \dot{\delta}(t) \leq 5.5\text{deg/s} \tag{23}$$

According to Reference [45], when the lateral force on the wheels reaches saturation, further steering adjustments do not affect the yaw rate. Thus, the yaw rate constraint is as follows:

$$-\frac{\mu g}{v_{y1}(t)} \leq \omega_{z1}(t) \leq \frac{\mu g}{v_{y1}(t)} \tag{24}$$

4.3. SOSMC Lower-Layer Controller

To address the nonlinear characteristics of the hydraulic system, such as gain fluctuations and leakage, a lower-layer controller based on SOSMC is designed [46,47]. This controller exhibits strong robustness, effectively managing system nonlinearities and uncertainties while reducing chattering to ensure smooth outputs. Leveraging its fast convergence, the system can track the upper-layer NMPC target torque in real time and adjust the steering wheel angle accordingly, achieving stable steering and precise path tracking for the UARR.

Based on Equations (10)–(12), (15), (17), and (18), the steering torque M_j and steering wheel angle θ_F exhibit a nonlinear functional relationship, given by the following:

$$M_j(\theta_F) = a(P_4(\theta_F) - P_3(\theta_F))(A_1 + A_2)\cos\delta + L_{f2}(P_4(\theta_F) + P_3(\theta_F))(A_1 - A_2)\sin\delta \tag{25}$$

The sliding surface $s(\theta_F,t)$ is defined as follows:

$$s(\theta_F, t) = \dot{e}(t) + \lambda e(t) \tag{26}$$

where $e(t) = M_j(\theta_F,t) - M_j{}^*(t)$ represents the tracking error, and $\lambda > 0$ is a design parameter regulating the system's dynamic response.

The control law is given by the following:

$$\ddot{\theta}_F(t) = \ddot{\theta}_{eq}(t) + u_{stw} \tag{27}$$

where $\ddot{\theta}_{eq}(t)$ is the equivalent control term, compensating for nonlinearities and enabling accurate tracking under ideal conditions:

$$\ddot{\theta}_{eq} = -\left(\frac{\partial M_j}{\partial \theta_F}\right)^{-1}\left[\frac{\partial^2 M_j}{\partial \theta_F^2}(\dot{\theta}_F)^2 - \ddot{M}_j^*(t) + \lambda\left(\frac{\partial M_j}{\partial \theta}\dot{\theta}_F - M_j^*(t)\right)\right] \tag{28}$$

The term u_{stw} represents the super-twisting control, enhancing robustness and reducing chattering:

$$u_{stw} = -k_1|s|^{1/2}sign(s) - k_2\int_0^t sign(s(\tau))d\tau \tag{29}$$

where k_1 and k_2 are control gains, with $k_1 > 0$ and $k_2 > 0$.

Combining the equivalent and super-twisting terms yields the complete control law:

$$\ddot{\theta}(t) = -\left(\frac{\partial M_j}{\partial \theta_F}\right)^{-1}\left[\frac{\partial^2 M_j}{\partial \theta_F^2}(\dot{\theta}_F)^2 - \ddot{M}_j^*(t) + \lambda\left(\frac{\partial M_j}{\partial \theta_F}\dot{\theta}_F - M_j^*(t)\right)\right] - k_1|s|^{1/2}sign(s) - k_2\int_0^t sign(s(\tau))d\tau \tag{30}$$

To prove stability, a Lyapunov function $V(s) = 1/2\, s^2$ is defined. Using the sliding surface and control law, it follows that

$$\dot{V}(s) = -k_1|s|^{3/2} - k_2|s| \tag{31}$$

Since $k_1 > 0$ and $k_2 > 0$, $V(s)$ is positive definite, and its derivative is negative semi-definite, thereby fulfilling the stability conditions.

4.4. ST-UKF Ground Adhesion Coefficient Observer

The variation in ground adhesion coefficient significantly affects the tracking control accuracy of UARR, especially on slippery and unstructured surfaces where adhesion uncertainty complicates system stability. Precise estimation of the ground adhesion coefficient is, therefore, crucial. In this context, the UKF [48,49] has proven effective due to its superior handling of nonlinear systems. Unlike the extended Kalman filter (EKF), UKF does not depend on Taylor expansion and Jacobian matrices but uses a set of sigma points to approximate the system state's distribution, achieving second-order estimation accuracy—ideal for complex nonlinear dynamics. However, UKF has a limitation due to its fixed weight coefficients throughout the filtering process. Under conditions of anisotropic road adhesion surfaces, these fixed weights for mean and covariance may inadequately capture rapid environmental changes, resulting in a prolonged influence of outdated data and reduced sensitivity to new state variations. To overcome this limitation, the strong tracking filter (STF) [50,51] concept is introduced. By incorporating a fading factor matrix and a constraint proportional factor into the UKF, the covariance matrix is dynamically adjusted in real time, mitigating the impact of outdated data and improving adaptability to environmental changes. The fading factor reduces the influence of historical data on estimation, allowing the filter to respond swiftly to system variations and maintain accurate state tracking. This modification ensures that residuals remain orthogonal across time instants, enhancing estimation accuracy and system robustness, particularly under abrupt changes.

Selecting the adhesion coefficients between the drum, rear wheels, and the ground as state variables, the state equation of the ST-UKF observer is given by the following:

$$x(t) = F(x(t), u(t)) + v(t) = \begin{bmatrix} 1 & 0 & 0 \\ 0 & 1 & 0 \\ 0 & 0 & 1 \end{bmatrix} \begin{bmatrix} \mu_f \\ \mu_{r1} \\ \mu_{r2} \end{bmatrix} + v(t) \tag{32}$$

The measurement equation of the adhesion coefficient observer is derived by combining the UARR dynamics Equations (1) and (2), the acceleration Equation (3), the velocity constraint Equations (4) to (6), and the normalized Dugoff tire forces (8) and (9), and assuming small-angle variations in the articulation angle δ:

$$y(t) = H(x(t), u(t)) + n(t) = \begin{bmatrix} \frac{F^0_{xf}}{m_f+m_r} & \frac{F^0_{xr1}}{m_f+m_r} & \frac{F^0_{xr2}}{m_f+m_r} \\ H(2,1) & H(2,2) & H(2,3) \\ H(3,1) & H(3,2) & H(3,3) \end{bmatrix} \begin{bmatrix} \mu_f \\ \mu_{r1} \\ \mu_{r2} \end{bmatrix} + \begin{bmatrix} 0 \\ U(2,1) \\ U(3,1) \end{bmatrix} M_j + n(t) \tag{33}$$

Here, $H(i, j)$ ($i = 2, 3$, $j = 1, 2, 3$) is defined in Appendix A. The vector $x(t) = [\mu_f, \mu_{r1}, \mu_{r2}]^T$ represents the adhesion coefficients to be estimated, $y(t) = \left[a_{fx}, a_{fy}, \dot{\omega}_{z1}\right]^T$ denotes the measured outputs, and $u(t) = [M_j]$ is the control input. $F(.)$ is the transition function, $H(.)$ is the output function, $v(t)$ represents process noise with zero mean and covariance matrix Q, and $n(t)$ is measurement noise with zero mean and covariance matrix R.

5. Control Strategy Validation and Performance Analysis

To comprehensively evaluate the effectiveness of the HCC strategy, this section first verifies the tracking performance of the lower-level SOSMC in a simulation environment. Then, real-vehicle experiments are conducted to systematically assess the controller's transient response and steady-state performance. Finally, further simulation studies analyze the impact of the ground adhesion coefficient observer on control effectiveness, with a particular focus on its adaptive performance under low-adhesion conditions.

5.1. SOSMC Tracking Performance Verification

A simulation experiment was designed to evaluate the tracking capability of SOSMC for the steering torque M_j computed by NMPC and to output the corresponding steering wheel angle. The tracking performance and the resulting steering wheel angle are shown in Figure 14a,b. From the perspective of transient response, despite the inherent dynamic lag and nonlinear effects of the hydraulic system, which cause delays and dynamic deviations in tracking, SOSMC still responds quickly to step changes in the target torque and tracks effectively. In terms of steady-state performance, the torque output by the controller remains consistent with the target torque, exhibiting minimal steady-state error. This clearly demonstrates that SOSMC provides smooth and robust control signals, ensuring system stability when handling complex nonlinear systems. Furthermore, Figure 11 shows no significant oscillations, which can be attributed to the inclusion of first- and second-order derivatives in the sliding surface design, effectively suppressing the chattering caused by pressure variations, hydraulic delays, and viscoelastic effects. Figure 14b further corroborates this, showing the smooth variation in the steering wheel angle.

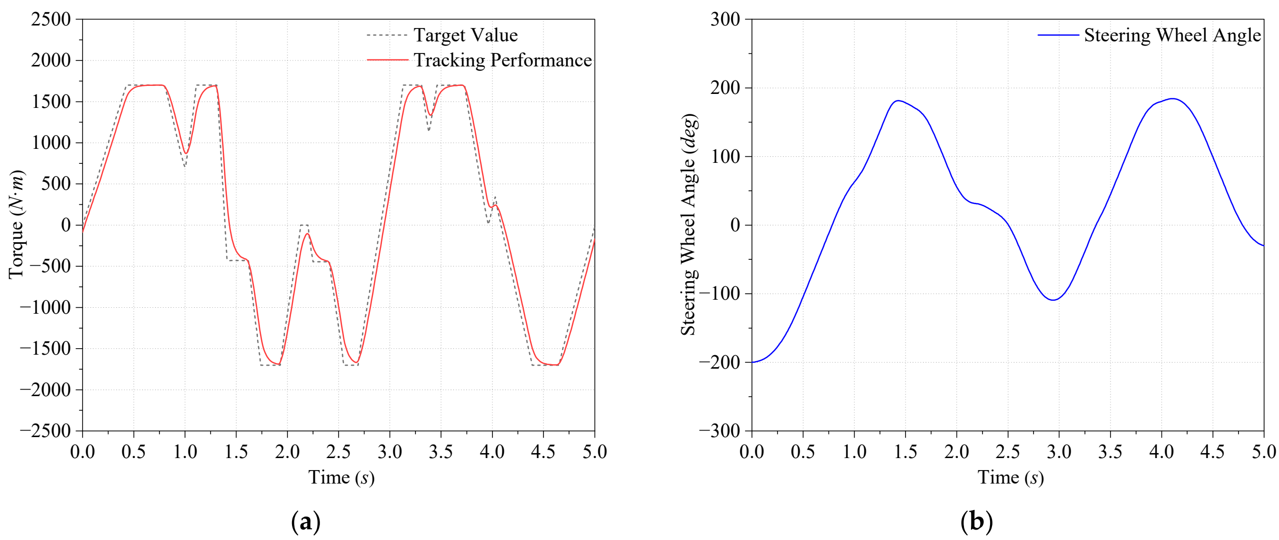

Figure 14. SOSMC tracking performance verification: (**a**) tracking target steering torque M_j; (**b**) corresponding steering wheel angle output.

5.2. HCC Transient and Steady-State Performance Validation

The HCC's tracking performance was evaluated under real-world engineering scenarios on a surface composed predominantly of soil with minor gravel content. Under dry conditions, the terrain behaves much like ordinary soil, whereas after rainfall, it transitions into a muddy, significantly more slippery surface, as shown in Figure 15.

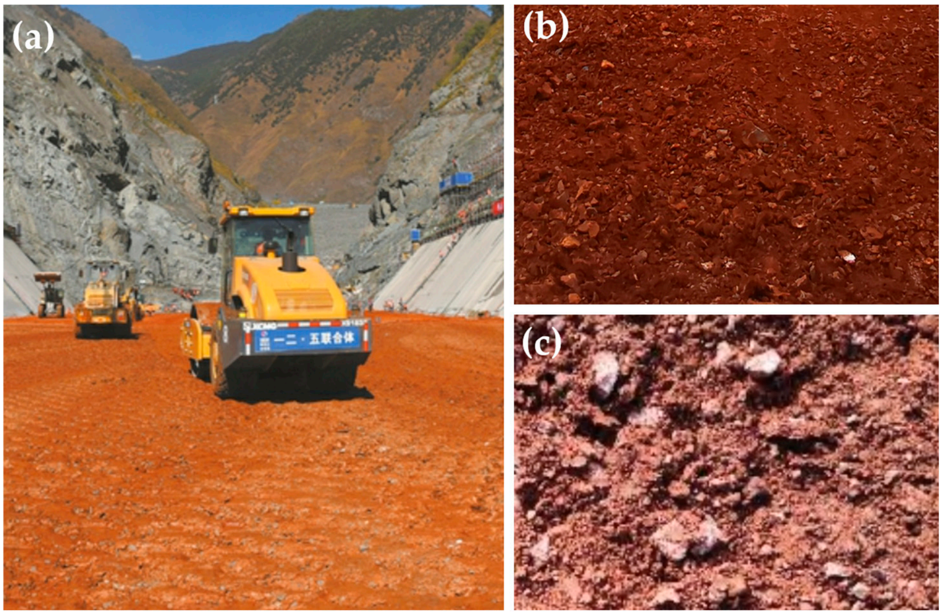

Figure 15. (**a**) Experimental scenario; (**b**) dry surface; (**c**) slippery surface.

5.2.1. Real-Vehicle Testing on Dry Gravelly Soil

1. An experiment was designed for UARR to track a step target at y = 2 m from (0, 0), with tracking deemed successful if the error is less than 5 cm, validating the transient response of the HCC. LQR and PID strategies were also compared.

Figure 16a illustrates the tracking performance of the three controllers. In terms of both transient response speed and tracking capability, HCC outperforms the others, reaching the target at x = 11.8 m and settling within the 5 cm allowable error range. LQR, while effective, lags slightly behind HCC. PID, although initially faster in transient response than LQR, suffers from overshoot when first approaching the target path, resulting in the slowest overall tracking performance. The HCC controller has almost no overshoot, while the LQR and PID controllers have overshoots of 6.92% and 8.28%, respectively.

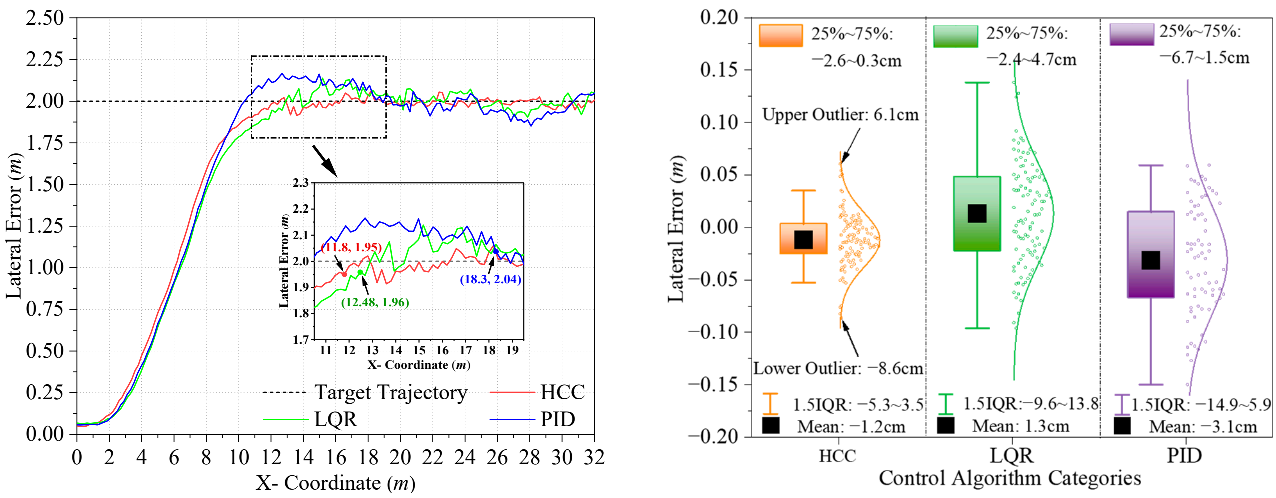

(**a**) (**b**)

Figure 16. Step-tracking experiment under dry conditions: (**a**) lateral error; (**b**) steady-state error distribution.

Figure 16b presents the steady-state error distribution after reaching the target path. For HCC, 50% of the steady-state error data lies within the range of −2.6 cm to 0.3 cm, with an interquartile range (IQR) spanning from −5.3 cm to 3.5 cm. The errors are tightly clustered, with the outliers limited to a maximum of 6.1 cm and a minimum of −8.6 cm, showcasing the high-precision tracking capability. In comparison, the upper and lower bounds of lateral error for LQR are 1.12 times and 2.26 times those of HCC, respectively, indicating a broader error distribution. PID demonstrates similar performance to LQR but with a slightly higher maximum lateral error—nearly 1 cm more than LQR. Furthermore, the average lateral distance errors for the three controllers are −1.2 cm, 1.3 cm, and −3.1 cm, respectively, with HCC yielding the smallest mean error.

2. An experiment was designed for UARR to track the straight line $y = 0$ starting from (0, 0), aiming to evaluate the steady-state performance of the controller. LQR and PID strategies were also compared.

Figure 17a shows the tracking performance. Overall, HCC exhibited the most stable lateral errors, with minimal fluctuations, demonstrating its ability to maintain the road roller consistently on the target path. LQR performed similarly to HCC, but with larger errors and more frequent significant fluctuations under the influence of ground conditions, indicating some delay and oscillations in response to disturbances. PID displayed the most noticeable fluctuations, with the largest error variation, reaching a peak of nearly 21 cm.

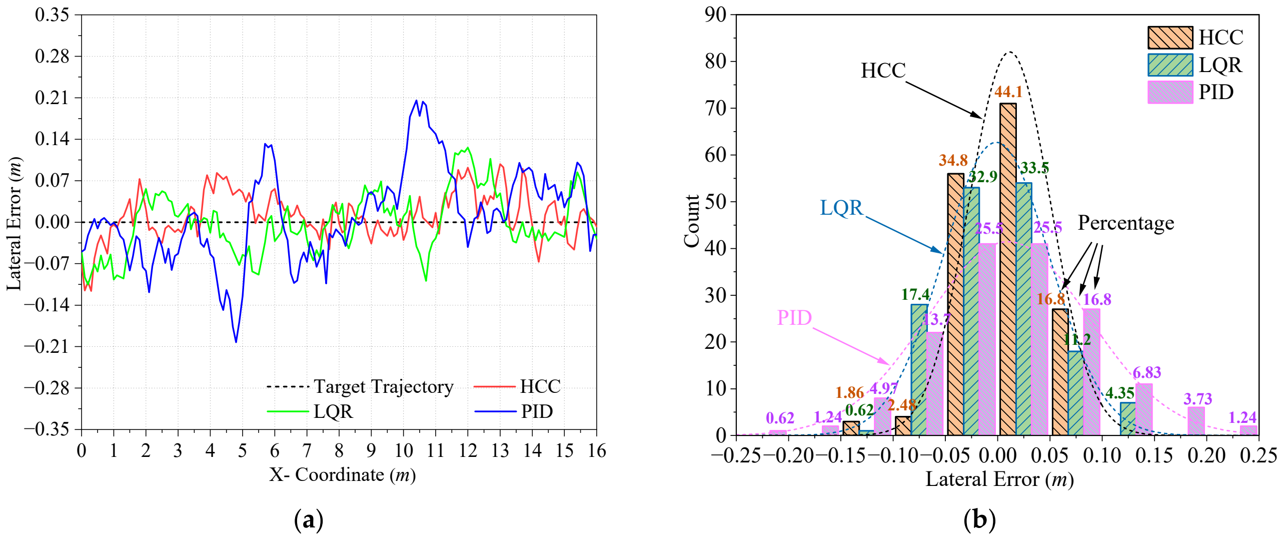

Figure 17. Straight line experiment under dry conditions: (**a**) lateral error; (**b**) lateral error distribution.

Figure 17b shows the lateral error distribution in the UARR straight line-tracking experiment. HCC achieves a high concentration of errors between −5 cm and 5 cm, accounting for 78.9%, with the largest percentage (44.1%) occurring near zero error. LQR has a more dispersed error distribution, with 66.4% of the errors falling within the range of −5 cm to 5 cm. PID has the most scattered distribution, with 18.63% of the errors exceeding 10 cm. Analysis indicates that HCC performs best on the dry gravel road surface, effectively minimizing error and ensuring stable path tracking, which is crucial for maintaining precise compaction paths and improving construction quality.

5.2.2. Real-Vehicle Testing on Wet and Slippery Gravelly Mud

1. An experiment was designed for UARR to track a step target at $y = 2$ m from (0, 0), with tracking deemed successful if the error is less than 5 cm, validating the transient response of the HCC. LQR and PID strategies were also compared.

Figure 18a shows the step-tracking performance of the three controllers under wet and slippery conditions. HCC performs the best, reaching the target and entering the allowable error range at x = 17.8 m. LQR is slightly slower, while PID, with a similar transient response to LQR, exhibits two overshoots, making it the slowest to enter the error range, only reaching the target at x = 22.2 m. Overall, despite all three controllers showing overshoot, with overshoot values of 8.024%, 12.938%, and 16.168%, respectively, HCC still demonstrates the strongest transient response, quickly stabilizing within the error range and maintaining stable tracking. LQR follows with a slightly slower response, while PID performs the worst, affecting vehicle stability.

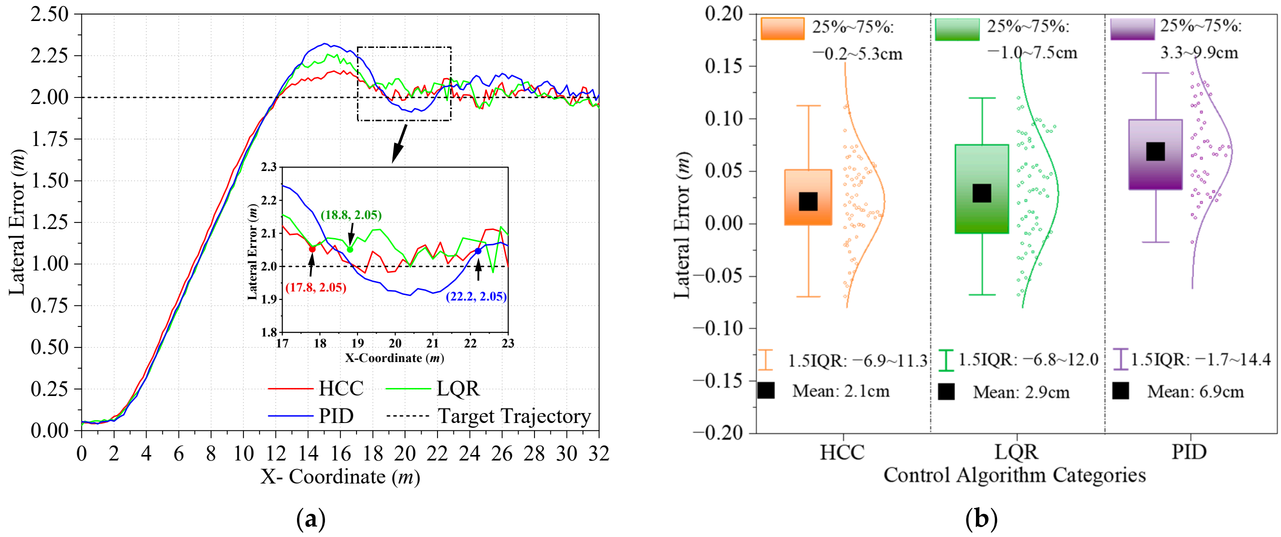

Figure 18. Step-tracking experiment under dry wet and slippery conditions: (**a**) lateral error; (**b**) steady-state error distribution.

Figure 18b shows the steady-state error distribution. For HCC, 50% of the steady-state errors fall between −0.2 cm and 5.3 cm, with an IQR of −6.9 cm to 11.3 cm. The errors are concentrated, indicating that HCC maintains high tracking accuracy under slippery conditions, with a mean error of 2.1 cm, demonstrating good steady-state performance. LQR shows a more dispersed error distribution, with a slightly higher mean than HCC. PID has the most unstable error distribution, with a significant positive bias, struggling to effectively control lateral errors under slippery conditions.

A comparison of Figures 16b and 18b reveals that whether under dry or slippery conditions, HCC consistently exhibits the most concentrated lateral error, demonstrating the best performance. Additionally, the wet and slippery conditions lead to an increase in mean error, with PID showing the largest error increase and performing the worst. In contrast, HCC maintains high control accuracy, showcasing strong robustness and adaptability to varying environmental conditions.

2. An experiment was designed for UARR to track the straight line y = 0 starting from (0, 0), aiming to evaluate the steady-state performance of the controller. LQR and PID strategies were also compared.

Figure 19a illustrates the lateral errors during the straight line-tracking task under slippery conditions. HCC demonstrates the most stable lateral error fluctuations, reflecting its superior control performance. This ability allows HCC to maintain the vehicle's adherence to the target path even on slippery surfaces, highlighting its robust disturbance rejection capability. In contrast, LQR exhibits noticeably larger errors compared to HCC, with considerable lag and fluctuations in certain segments, primarily due to the impact of the slippery ground. PID, however, shows the poorest performance, characterized by the largest error magnitude and multiple instances of significant deviation, indicating a clear lack of stability under these conditions.

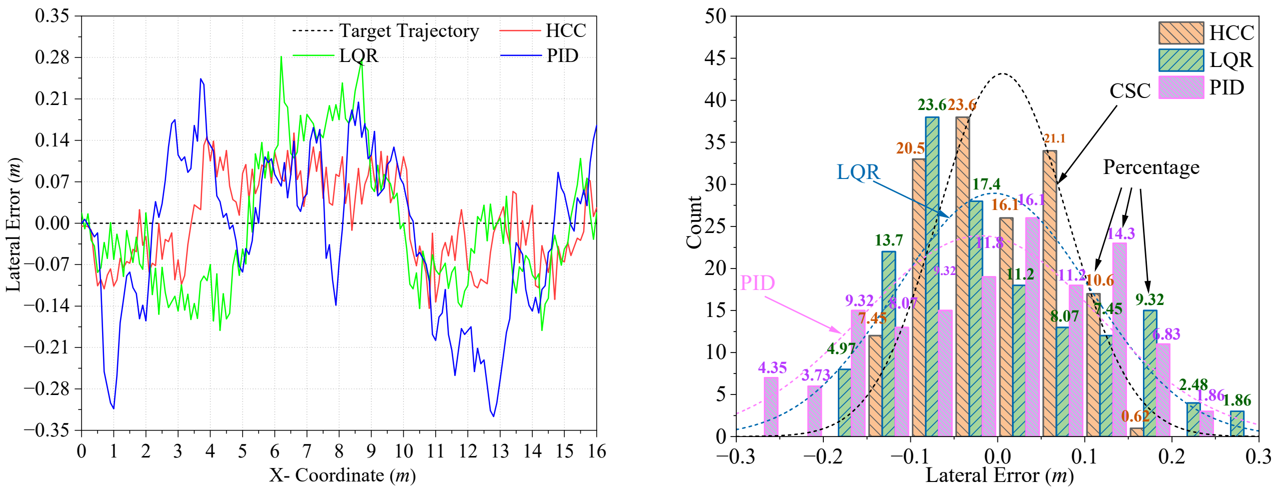

(a) **(b)**

Figure 19. Straight line experiment under wet and slippery conditions: (**a**) lateral error; (**b**) lateral error distribution.

Figure 19b shows the lateral distance error distribution in the wet and slippery straight line test. For HCC, 81.3% of the errors are confined to the range of −10 cm to 10 cm, indicating a high degree of concentration. The maximum lateral error for HCC is approximately 16 cm, accounting for only 0.62%. In contrast, LQR has only 4.97% of the errors within the same range, with a maximum lateral error of 27 cm, and 4.34% of the errors exceeding 20 cm. These more dispersed errors and extreme values highlight that LQR is less stable in handling external disturbances under slippery conditions compared to HCC. Overall, PID shows the poorest performance.

A comparison of Figures 17b and 19b reveals significant differences in the lateral error performance of the controllers under dry and slippery road conditions. In the dry tests, all three controllers exhibit relatively small lateral errors, with HCC performing the best. However, under slippery conditions, the errors for all the controllers increase substantially. Despite this, HCC still maintains good tracking performance, with a relatively concentrated error distribution, demonstrating its robustness and strong adaptability under challenging road conditions.

5.3. Verification of HCC Adaptive Performance Under ST-UKF Observer

The real-vehicle tests of HCC reveal a significant increase in lateral error when transitioning from dry to wet and slippery surfaces, highlighting the pronounced impact of variations in the ground adhesion coefficient (μ) on control performance. To mitigate this, a ground adhesion coefficient observer based on the ST-UKF is introduced. A simulation experiment is conducted in which the UARR tracks the straight line $y = 0$, starting from the point (0, 0). In the simulation, the road is characterized by a high adhesion coefficient of $\mu = 0.8$ over the first 10 m, followed by a low adhesion coefficient of $\mu = 0.35$ over the next 20 m. Disturbances are also introduced to simulate surface irregularities. This simulation aims to assess the improvement in the control performance of HCC when employing the ground adhesion coefficient observer and to compare it with LQR and PID controllers.

Figure 20 presents the estimated ground adhesion coefficients. Under both high and low adhesion conditions, the estimated values closely track the set values. This is attributed to the introduction of the forgetting factor matrix and constraint proportional factors, which allow for the real-time adjustment of the covariance matrix, reducing the weight of old data and increasing the influence of new data. To assess the accuracy of the adhesion coefficient estimates and their impact on lateral error, the Root Mean Squared Error (RMSE) is used, as shown in Equation (A6).

$$REMS = \sqrt{\frac{1}{n}\sum_{i=1}^{n}(y_i - \hat{y}_i)^2} \tag{34}$$

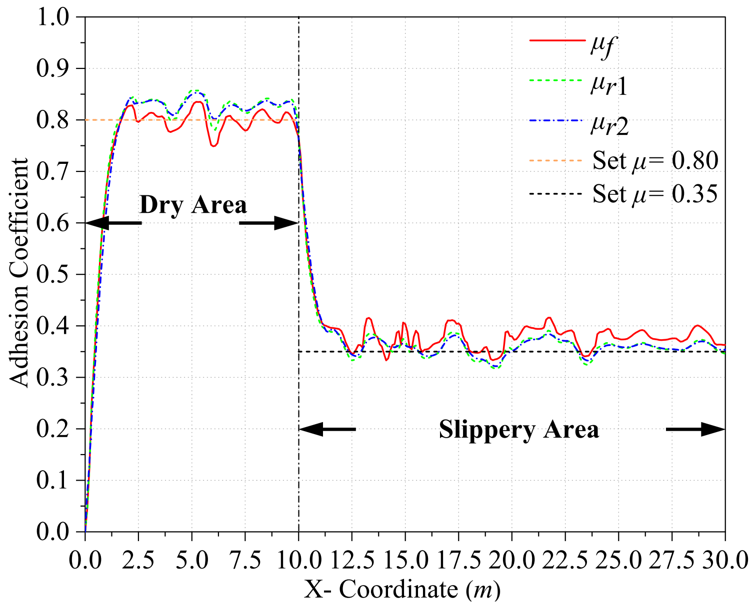

Figure 20. Ground surface adhesion coefficient estimation based on ST-UKF.

Here, n is the number of samples, and y_i and $\hat{y}_i$ are the i-th simulated and set values, respectively.

In the high-adhesion region, the estimated μ reaches the set value of 0.8 after approximately 1.6 m. In the low-adhesion region, however, it takes about 2.5 m to track the set value of 0.35, indicating a longer response distance in this condition, as in Figure 21. The REMS and mean values are presented in Table 4. The RMSE metric quantifies the tracking error of the ST-UKF observer, while the mean value's proximity to the set value reflects both the accuracy and stability of the observer under varying adhesion conditions. In the high-adhesion region, the drum exhibits the smallest RMSE and the mean value closely matches the set value, demonstrating high accuracy in estimating the adhesion coefficient due to the large contact area. In contrast, in the low-adhesion region, the rear wheel's estimates are more accurate, attributed to its material flexibility, which allows better adaptation to low-adhesion surfaces, reducing estimation errors. However, the drum's larger contact area leads to a greater tendency for slip, increasing observation errors.

Table 4. REMS and mean of ground adhesion coefficient estimated by ST-UKF.

Drum/Rear Wheel	High Adhesion Coefficient RMSE	High Adhesion Coefficient Mean Value	High Adhesion Coefficient RMSE	High Adhesion Coefficient Mean Value
Drum	0.01895	0.80048	0.03286	0.37611
Left Rear Wheel	0.03322	0.82873	0.01841	0.35780
Right Rear Wheel	0.03067	0.82782	0.01590	0.357951

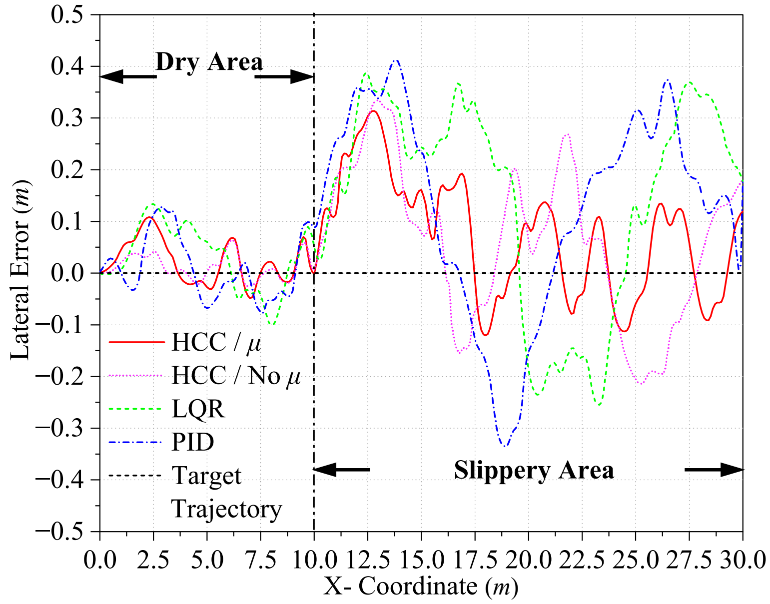

Figure 21. Comparison of lateral errors across controllers on roads with varying adhesion coefficients.

Figure 22 presents the distribution of lateral distance errors for three controllers during straight line tracking on roads with varying adhesion coefficients. In the high-adhesion region, the HCC without adhesion coefficient estimation exhibits smaller lateral errors compared to its counterpart with estimation. This difference arises because the former assumes a constant adhesion coefficient (μ) of 0.8, whereas the latter introduces disturbances in the simulation, causing the estimated coefficient to fluctuate slightly around the set value, resulting in marginally larger lateral errors. Despite this, the HCC with adhesion coefficient estimation still achieves a maximum error of only 10.8 cm, with a concentrated error distribution, maintaining a high level of precision. This performance clearly surpasses that of both LQR and PID.

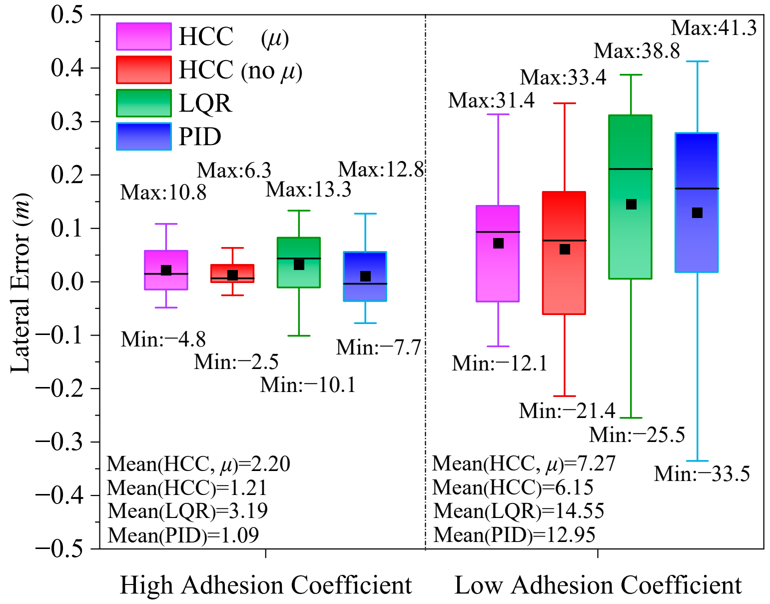

Figure 22. Lateral error distribution of different controllers under varying adhesion coefficients.

In the low-adhesion region, the HCC with μ estimation significantly outperforms the version without estimation. The error range for the former is −12.1 to 31.4 cm, while the latter spans from −21.4 to 33.4 cm, reflecting a 20.62% reduction in the error range and a 16.31% decrease in RMSE. This indicates that under wet and slippery conditions, the online estimation of the adhesion coefficient effectively reduces lateral errors and enhances path-tracking accuracy.

In contrast, owing to LQR's reliance on a linear tire model and the absence of an adhesion coefficient parameter, the maximum error in the low-adhesion region reaches 38.8 cm. The PID controller performs even less favorably, with a maximum error exceeding 40 cm and exhibiting multiple instances of substantial overshoot, resulting in significant deviations from the desired path. The RMSE values presented in Table 5 underscore the critical importance of the online estimation of the ground adhesion coefficient, particularly in enhancing the controller's steady-state performance under slippery conditions. The superior adaptability of HCC compared to LQR and PID lies in its reliance on the more accurate dynamics model proposed in this study. This enables HCC to effectively predict excessive overshoots and implement timely adjustments before they occur. As a result, the UARR controlled by HCC exhibits higher oscillation frequencies compared to the other two algorithms. In Figure 20, in the low-adhesion region, HCC (with μ estimation) adjusts approximately every 3.5 m, whereas LQR and PID respond more slowly. This demonstrates the enhanced adaptability and precision of HCC in managing trajectory deviations under challenging conditions.

Table 5. RMSE of lateral error for controllers on roads with varying adhesion coefficients. (The symbol ''↓'' indicates a decrease).

Controller	High Region (RMSE)	Low Region (RMSE)
HCC (μ estimated)	4.6321	13.3159 (2.595 cm, 16.31% ↓)
HCC (no μ)	2.6162	15.9109
LQR	6.9527	24.5419
PID	6.1526	23.3334

6. Conclusions

In this paper, an HCC architecture incorporating real-time ground adhesion coefficient observation is proposed to enhance the path-tracking performance of UARR. The proposed framework was validated through both simulations and real-vehicle experiments:

- Real-vehicle experiments were conducted on wet dirt and gravel roads to validate the 4-DOF dynamic model. Results revealed yaw angle correlation coefficients of 95.58% and 97.22%, longitudinal correlations of 97.18% and 97.59%, and lateral correlations of 92.84% and 91.81%, respectively. These outcomes demonstrate the model's accuracy and reliability.
- Simulation assessed the tracking capability of the SOSMC for the upper-layer controller's steering torque output. Findings showed that SOSMC delivers smooth and robust control signals, maintaining system stability under complex nonlinear conditions.
- The HCC's performance was evaluated under dry and wet gravel soil road conditions. Compared to LQR and PID, HCC exhibited the fastest response time and smallest steady-state error in both scenarios. However, during the step-tracking experiment on wet surfaces, the response time was 6 s slower than under dry conditions. In straight line-tracking tests, the proportion of steady-state errors exceeding 10 cm was 16.81% higher on wet surfaces, highlighting the significant impact of the ground adhesion coefficient on HCC performance. Additionally, the proposed HCC algorithm has undergone extensive field testing in an engineering project, accumulating over 80 km of operation over three months.
- Incorporating the ST-UKF for real-time ground adhesion coefficient observation reduced the steady-state error on wet surfaces by 20.62%. This highlights that the

real-time estimation of adhesion coefficients significantly enhances HCC's robustness and adaptability to environmental adaptability.

7. Future Work

In this paper, future research will further investigate the applicability of the proposed control approach for UARR under diverse climatic conditions and complex terrains to validate its generalizability and robustness. Additionally, efforts will be directed toward extending the HCC strategy to other types of unmanned vehicle systems, evaluating its practical effectiveness across different application scenarios. Furthermore, the possibility of integrating more advanced methods, such as reinforcement learning, into the control system will be explored to enhance its adaptability. These studies aim to provide broader support for the advancement of unmanned driving technologies across various fields.

Author Contributions: Conceptualization, W.Q. and H.X.; methodology, W.Q. and W.Y.; software, W.Q., Q.X. and W.Y.; resources, W.Q. and Q.X.; validation, W.Q. and Q.X.; formal analysis, W.Q.; investigation, W.Q.; data curation, W.Q. and W.Y.; writing—original draft preparation, W.Q.; writing—review and editing, W.Q. and W.Y.; visualization, W.Q. and W.Y.; supervision, H.X.; project administration, W.Q.; funding acquisition, H.X. All authors have read and agreed to the published version of the manuscript.

Funding: This work was supported by the National Key Research and Development Program of China under Grant 2022YFE0100100.

Data Availability Statement: In this study, simulation data were obtained from causality-based physical modeling, while real-vehicle experimental data were collected using the test platform described in Section 2.

Acknowledgments: This research was initiated by the Advanced Power and Intelligent Vehicle Control Group at Tianjin University and was financially supported by the National Key R&D Program of China. The authors extend their sincere gratitude for this support.

Conflicts of Interest: The authors declare no conflicts of interest.

Abbreviations

UARR	unmanned articulated road roller
HCC	hierarchical cascaded control
NMPC	nonlinear model predictive controller
4-DOF	4-degree-of-freedom
SOSMC	second-order sliding mode controller
ST-UKF	strong-tracking unscented Kalman filter
NEM	Newton–Euler method

Appendix A

$$A = \begin{pmatrix} \cos\delta & -\sin\delta & \frac{m_r L_{f2}\sin\delta}{m_f+m_r} & -\frac{2m_r L_{r2}}{m_f+m_r}\omega_{z1} \\ \sin\delta & \cos\delta & -\frac{m_r(L_{f2}\cos\delta+L_{r2})}{m_f+m_r} & 0 \\ 0 & \frac{m_f L_{f2}}{I_{z1}} & 1 & 0 \\ -\frac{m_f L_{r2}\sin\delta}{I_{z2}} & -\frac{m_f L_{r2}\cos\delta}{I_{z2}} & -1 & 0 \end{pmatrix} \tag{A1}$$

$$\dot{X} = \begin{pmatrix} \dot{v}_{x1} \\ \dot{v}_{y1} \\ \dot{\omega}_{z1} \\ \dot{\delta} \end{pmatrix} \tag{A2}$$

$$b = \begin{pmatrix} 0 \\ 0 \\ -\frac{1}{I_{z1}} \\ -\frac{1}{I_{z2}\cos\delta} \end{pmatrix} \tag{A3}$$

$$f(x) = \begin{pmatrix} -v_{x1}\omega_{z1}\sin\delta - v_{y1}\omega_{z1}\cos\delta + \frac{m_r(L_{f2}\cos\delta + L_{r2})}{m_f+m_r}\omega_{z1}^2 + \frac{m_r L_{r2}}{m_f+m_r}\dot{\delta}^2 + \frac{-F_{xf}\cos\delta + F_{yf}\sin\delta - F_{xr1} - F_{xr2}}{m_f+m_r} \\ v_{x1}\omega_{z1}\cos\delta - v_{y1}\omega_{z1}\sin\delta + \frac{m_r L_{f2}}{m_f+m_r}\omega_{z1}^2\sin\delta + \frac{m_r L_{r2}}{m_f+m_r}\ddot{\delta} - \frac{F_{xf}\sin\delta + F_{yf}\cos\delta + F_{yr1} + F_{yr2}}{m_f+m_r} \\ \frac{m_f L_{f2}}{I_{z1}} v_{x1}\omega_{z1} + \frac{L_{f1} - L_{f2}}{I_{z1}} F_{yf} \\ \frac{m_f L_{r2}}{I_{z2}}(v_{y1}\sin\delta - v_{x1}\cos\delta)\omega_{z1} + \ddot{\delta} + \frac{L_{r2}}{I_{z2}}(F_{xf}\sin\delta + F_{yf}\cos\delta) + \frac{e}{I_{z2}}(F_{xr1} - F_{xr2}) - \frac{L_{r1}}{I_{z2}}(F_{yr1} + F_{yr2}) \end{pmatrix} \tag{A4}$$

$$F_{yf/ri} = \mu F_{zf/r} C_{yf/r} \frac{\tan(\alpha_{1/2})}{1 - S_{xf/ri}} f(\kappa) \tag{A5}$$

$$F_{xf/ri} = \mu F_{zf/r} C_{xf/r} \frac{S_{xf/ri}}{1 - S_{xf/ri}} f(\kappa) \tag{A6}$$

$$f(\kappa) = \begin{cases} 1, if\ \kappa \geq 1 \\ (2-\kappa)\kappa,\ if\ \kappa < 1 \end{cases} \tag{A7}$$

$$\kappa = \frac{(1 - S_{xf/ri})}{2\sqrt{(C_{xf/r}S_{xf/ri})^2 + (C_{yf/r}\tan\alpha_{1/2})^2}} \tag{A8}$$

$$S_{xf/ri} = \frac{\left|v_{xj} - \omega_{f/r}R_{f/r}\right|}{\max\left|v_{xj}, \omega_{f/r}R_{f/r}\right|} \tag{A9}$$

$$\begin{cases} \alpha_1 = \frac{v_{y1} - L_{f1}\omega_{z1}}{v_{x1}} \\ \alpha_2 = \frac{v_{y2} - L_{r1}\omega_{z2}}{v_{x2} - e\omega_{z2}} \end{cases} \tag{A10}$$

$$\begin{cases} \begin{cases} H(2,1) = HI_{z2}\left[I_{z1} + m_r\left(L_{f2}^2 + L_{r2}^2 - L_{f1}L_{f2}\right)\right]F_{yf}^0 \\ H(2,2) = HI_{z1}\left[m_r L_{r2} e F_{xr1}^0 + (I_{z2} - m_r L_{r1} L_{r2})F_{yr1}^0\right] \\ H(2,3) = HI_{z1}\left[-m_r L_{r2} e F_{xr2}^0 + (I_{z2} - m_r L_{r1} L_{r2})F_{yr2}^0\right] \end{cases} \\ \begin{cases} H(3,1) = Hm_f m_r L_{r2}^2 I_{z2}\left(\frac{L_{f2} - L_{f1}}{m_f L_{r2}^2} - \frac{L_{f1}}{m_r L_{r2}^2} - \frac{L_{f2}}{I_{z1}} + \frac{L_{f2} - L_{f1}}{I_{z2}}\right)F_{yf}^0 \\ H(3,2) = -Hm_f L_{f2}\left[m_r L_{r2} e F_{xr1}^0 + (I_{z2} - m_r L_{r1} L_{r2})F_{yr1}^0\right] \\ H(3,3) = Hm_f L_{f2}\left[m_r L_{r2} e F_{xr2}^0 - (I_{z2} - m_r L_{r1} L_{r2})F_{yr2}^0\right] \end{cases} \\ \begin{cases} U(2,1) = H(m_r I_{z2} L_{f2} - m_r I_{z1} L_{r2}) \\ U(3,1) = H\left[(m_f + m_r)I_{z2} + m_f m_r L_{r2}(L_{f2} + L_{r2})\right] \end{cases} \end{cases} \tag{A11}$$

References

1. Gao, H.; Wang, J.; Cui, B.; Wang, X.; Lin, W. An innovation gain-adaptive Kalman filter for unmanned vibratory roller positioning. *Measurement* **2022**, *203*, 111900. [CrossRef]
2. Huang, H.; Wang, X.; Hu, Y.; Tan, P. Accuracy Analysis of Visual Odometer for Unmanned Rollers in Tunnels. *Electronics* **2023**, *12*, 4202. [CrossRef]
3. Kim, H.-J.; Kim, J.-Y.; Kim, J.-W.; Kim, S.-K.; Na, W.S. Unmanned Aerial Vehicle-Based Automated Path Generation of Rollers for Smart Construction. *Electronics* **2023**, *13*, 138. [CrossRef]
4. Shi, M.; Wang, J.; Li, Q.; Cui, B.; Guan, S.; Zeng, T. Accelerated earth-rockfill dam compaction by collaborative operation of unmanned roller fleet. *J. Constr. Eng. Manag.* **2022**, *148*, 04022046. [CrossRef]

5. Song, E.-B.; Zhang, X. Research on the path optimization of unmanned rolling impaction for high embankment of airport. *Jpn. Geotech. Soc. Spec. Publ.* **2020**, *8*, 142–148. [CrossRef]
6. Carabin, G.; Gasparetto, A.; Mazzetto, F.; Vidoni, R. Design, implementation and validation of a stability model for articulated autonomous robotic systems. *Robot. Auton. Syst.* **2016**, *83*, 158–168. [CrossRef]
7. Yang, M.; Bian, Y.; Liu, G.; Zhang, H. Path tracking control of an articulated road roller with sideslip compensation. *IEEE Access* **2020**, *8*, 127981–127992. [CrossRef]
8. Zhang, J. Stability Analysis of Vibratory Roller. *J. Hunan Ind. Polytech.* **2022**, *22*, 22–25.
9. Zhang, Q.; Liu, T.; Zhang, Z.; Huangfu, Z.; Li, Q.; An, Z. Unmanned rolling compaction system for rockfill materials. *Autom. Constr.* **2019**, *100*, 103–117. [CrossRef]
10. Bian, Y.; Fang, X.; Yang, M.; Zhao, Z. Automatic rolling control for unmanned vibratory roller based on fuzzy algorithm. *J. Tongji Univ. Nat. Sci.* **2017**, *45*, 1830–1838.
11. Song, K.; Xie, H. Path-following control for unmanned rollers: A composite disturbance rejection-based framework. In Proceedings of the 2020 IEEE 9th Data Driven Control and Learning Systems Conference (DDCLS), Liuzhou, China, 19–21 June 2020; pp. 432–437.
12. Xie, H.; Xu, Q.; Song, K. Layered disturbance rejection path-following control with geometry-based feedforward for unmanned rollers. *Proc. Inst. Mech. Eng. Part D J. Automob. Eng.* **2023**, *237*, 1435–1453. [CrossRef]
13. Fang, X.; Bian, Y.; Yang, M.; Liu, G. Development of a path following control model for an unmanned vibratory roller in vibration compaction. *Adv. Mech. Eng.* **2018**, *10*, 1687814018773660. [CrossRef]
14. Deng, Z.-w.; Jin, Y.-h.; Gao, W.; Wang, B.-h. A closed-loop directional dynamics control with LQR active trailer steering for articulated heavy vehicle. *Proc. Inst. Mech. Eng. Part D J. Automob. Eng.* **2023**, *237*, 2741–2758. [CrossRef]
15. Tian, J.; Zeng, Q.; Wang, P.; Wang, X. Active steering control based on preview theory for articulated heavy vehicles. *PLoS ONE* **2021**, *16*, e0252098. [CrossRef] [PubMed]
16. Emheisen, M.A.; Emirler, M.T.; Ozkan, B. Lateral stability control of articulated heavy vehicles based on active steering system. *Int. J. Mech. Eng. Robot. Res.* **2022**, *11*, 575–582. [CrossRef]
17. Sun, N.; Zhang, W.; Yang, J. Integrated Path Tracking Controller of Underground Articulated Vehicle Based on Nonlinear Model Predictive Control. *Appl. Sci.* **2023**, *13*, 5340. [CrossRef]
18. Sharma, T.; He, Y. Design of a tracking controller for autonomous articulated heavy vehicles using a nonlinear model predictive control technique. *Proc. Inst. Mech. Eng. Part K J. Multi-Body Dyn.* **2024**, 14644193241232353. [CrossRef]
19. Zhong, S.; Peng, D.; Huang, B.; Ma, L. Path-Tracking Ability of the ASV on Different Adhesion Coefficient Roads Based on Slide Mode Control. *Electronics* **2023**, *13*, 105. [CrossRef]
20. Hu, K.; Cheng, K. Trajectory planning for an articulated tracked vehicle and tracking the trajectory via an adaptive model predictive control. *Electronics* **2023**, *12*, 1988. [CrossRef]
21. Ji, P.; Wu, J. Soft Measurement of Road Adhesion Coefficient Volumetric Kalman Filtering. *Acad. J. Sci. Technol.* **2023**, *7*, 131–137. [CrossRef]
22. Qi, G.; Fan, X.; Li, H. A comparative study of the unscented Kalman filter and particle filter estimation methods for the measurement of the road adhesion coefficient. *Mech. Sci.* **2022**, *13*, 735–749. [CrossRef]
23. Quan, L.; Chang, R.; Guo, C. Vehicle State and Road Adhesion Coefficient Joint Estimation Based on High-Order Cubature Kalman Algorithm. *Appl. Sci.* **2023**, *13*, 10734. [CrossRef]
24. Li, C.; Liu, P.X.; Xie, Z.; Li, Z.; Huan, H. Road Adhesion Coefficient Estimation Based on Vehicle-Road Coordination and Deep Learning. *J. Adv. Transp.* **2023**, *2023*, 3633058. [CrossRef]
25. Xiao, Y.; Zhang, X.; Xu, X.; Liu, X.; Liu, J. Deep neural networks with Koopman operators for modeling and control of autonomous vehicles. *IEEE Trans. Intell. Veh.* **2022**, *8*, 135–146. [CrossRef]
26. Ma, J.; Xie, H.; Song, K.; Liu, H. Self-optimizing path tracking controller for intelligent vehicles based on reinforcement learning. *Symmetry* **2021**, *14*, 31. [CrossRef]
27. Wu, X.; Lin, L.; Chen, J.; Du, S. A fast predictive control method for vehicle path tracking based on a recurrent neural network. *IEEE Access* **2024**. [CrossRef]
28. Sierra-Garcia, J.E.; Santos, M. Combining reinforcement learning and conventional control to improve automatic guided vehicles tracking of complex trajectories. *Expert Syst.* **2024**, *41*, e13076. [CrossRef]
29. Yao, J.; Ge, Z. Path-tracking control strategy of unmanned vehicle based on DDPG algorithm. *Sensors* **2022**, *22*, 7881. [CrossRef]
30. Rajamani, R. *Vehicle Dynamics and Control*; Springer Science & Business Media: Berlin/Heidelberg, Germany, 2011.
31. Kissai, M.; Monsuez, B.; Tapus, A.; Martinez, D. A new linear tire model with varying parameters. In Proceedings of the 2017 2nd IEEE International Conference on Intelligent Transportation Engineering (ICITE), Singapore, 1–3 September 2017; pp. 108–115.
32. Guo, K.; Ren, L. *A Non-Steady and Non-Linear Tire Model Under Large Lateral Slip Condition*; SAE Technical Paper: Warrendale, PA, USA, 2000; ISSN 0148-7191.

33. Zhang, H.; Yao, J.; Tian, S. Model Predictive Control for Trajectory Planning Considering Constraints on Vertical Load Variation. *Electronics* **2024**, *13*, 1488. [CrossRef]
34. Dugoff, H.; Fancher, P.S.; Segel, L. *Tire Performance Characteristics Affecting Vehicle Response to Steering and Braking Control Inputs*; National Academies: Washington, DC, USA, 1969.
35. Pacejka, H.B.; Bakker, E. The magic formula tyre model. *Veh. Syst. Dyn.* **1992**, *21*, 1–18. [CrossRef]
36. Singh, K.B. Vehicle sideslip angle estimation based on tire model adaptation. *Electronics* **2019**, *8*, 199. [CrossRef]
37. Wang, G.; Bai, G.; Meng, Y.; Liu, L.; Gu, Q.; Ma, Z. A Hierarchical Estimation Method for Road Friction Coefficient Combining Single-Step Moving Horizon Estimation and Inverse Tire Model. *Electronics* **2023**, *12*, 525. [CrossRef]
38. Nishihara, O.; Masahiko, K. Estimation of road friction coefficient based on the brush model. *J. Dyn. Sys. Meas. Control.* **2011**, *133*, 041006. [CrossRef]
39. Mei, Z.; Xiao, A.; Mei, J.; Hu, J.; Zhang, P. Experimental Study on Interface Frictional Characteristics between Sand and Steel Pipe Jacking. *Appl. Sci.* **2023**, *13*, 2016. [CrossRef]
40. He, R.; Jimenez, E.; Savitski, D.; Sandu, C.; Ivanov, V. Investigating the parameterization of dugoff tire model using experimental tire-ice data. *SAE Int. J. Passeng. Cars-Mech. Syst.* **2016**, *10*, 83–92. [CrossRef]
41. Villano, E.; Lenzo, B.; Sakhnevych, A. Cross-combined UKF for vehicle sideslip angle estimation with a modified Dugoff tire model: Design and experimental results. *Meccanica* **2021**, *56*, 2653–2668. [CrossRef]
42. Deng, T.; Lin, C.; Luo, J.; Chen, B. NSGA-II multi-objectives optimization algorithm for energy management control of hybrid electric vehicle. *Proc. Inst. Mech. Eng. Part D J. Automob. Eng.* **2019**, *233*, 1023–1034. [CrossRef]
43. Yusoff, Y.; Ngadiman, M.S.; Zain, A.M. Overview of NSGA-II for optimizing machining process parameters. *Procedia Eng.* **2011**, *15*, 3978–3983. [CrossRef]
44. Yin, J. Steering mechanics and steering power about articulated single-drum vibratory road roller. *Constr. Mech.* **2007**, *3*, 20–23.
45. Wu, X.; Zhou, B.; Wen, G.; Long, L.; Cui, Q. Intervention criterion and control research for active front steering with consideration of road adhesion. *Veh. Syst. Dyn.* **2018**, *56*, 553–578. [CrossRef]
46. Benamor, A.; Chrifi-Alaoui, L.; Chabaane, M.; Bussy, P.; Messaoud, H. A new second order sliding mode control approach for coupled MIMO nonlinear uncertain systems. In Proceedings of the 2011 19th Mediterranean Conference on Control & Automation (MED), Corfu, Greece, 20–23 June 2011; pp. 527–532.
47. Yusop, M.; Ariff, M.H.M.; Zamzuri, H.; Mazlan, S.A. Longitudinal slip control using magnetorheological brake via second order sliding mode controller. In Proceedings of the 2015 IEEE International Conference on Control System, Computing and Engineering (ICCSCE), Penang, Malaysia, 27–29 November 2015; pp. 563–568.
48. Wan, E.A.; Van Der Merwe, R. The unscented Kalman filter for nonlinear estimation. In Proceedings of the IEEE 2000 Adaptive Systems for Signal Processing, Communications, and Control Symposium (Cat. No. 00EX373), Lake Louise, AB, Canada, 1–4 October 2000; pp. 153–158.
49. Wang, Y.; Chang, Z.; Cai, Y.; Shang, Y.; Gao, F.; Huang, J. Road Adhesion Coefficient Estimation Based on Adaptive Unscented Kalman Filter. *Eng. Lett.* **2024**, *32*, 10.
50. Ping, X.; Cheng, S.; Yue, W.; Du, Y.; Wang, X.; Li, L. Adaptive estimations of tyre–road friction coefficient and body's sideslip angle based on strong tracking and interactive multiple model theories. *Proc. Inst. Mech. Eng. Part D J. Automob. Eng.* **2020**, *234*, 3224–3238. [CrossRef]
51. Xiong, H.; Tang, J.; Xu, H.; Zhang, W.; Du, Z. A robust single GPS navigation and positioning algorithm based on strong tracking filtering. *IEEE Sens. J.* **2017**, *18*, 290–298. [CrossRef]